END
DATE
FILMED
6-81
DTIC

1.0

2.8   2.5

3.2   2.2

3.6

4.0   2.0

1.1

1.8

1.25   1.4   1.6

MICROCOPY RESOLUTION TEST CHART

NATIONAL BUREAU OF STANDARDS

LEVEL

(12)

RESEARCH AND DEVELOPMENT TECHNICAL REPORT
CORADCOM-78-2402-F

(6) III-V HETEROSTRUCTURE AVALANCHE PHOTODIODE
MODULES FOR FIBER OPTIC COMMUNICATION LINKS
IN THE 1.0 TO 1.3 MICROMETER SPECTRAL RANGE.

DTIC
ELECTE
JUN 1 1981

C

(10) R. Yeats and K. Von Dessonneck

Solid State Laboratory
Varian Associates, Inc.
611 Hansen Way
Palo Alto, CA 94303

(11) 1 Jan 81   (12) 69

(9) Final Report, Feb 78 — May 80,

(15) DAAB17-78-C-2402

Approved for public release; distribution unlimited.

(16) 1L16 2 QLAH12

CORADCOM
U S ARMY COMMUNICATIONS RESEARCH & DEVELOPMENT COMMAND
FORT MONMOUTH, NEW JERSEY 07703

409910

REPORT DOCUMENTATION PAGE		READ INSTRUCTIONS BEFORE COMPLETING FORM
1. REPORT NUMBER CORADCOM-78-2402-F	2. GOVT ACCESSION NO. AD-A0-99506	3. RECIPIENT'S CATALOG NUMBER ----
4. TITLE *(and Subtitle)* III-V Heterostructure Avalanche Photodiode Modules for Fiber Optic Communication Links in the 1.0 to 1.3 Micrometer Spectral Range		5. TYPE OF REPORT & PERIOD COVERED Final Report February 1978--May 1980
		6. PERFORMING ORG. REPORT NUMBER
7. AUTHOR(s) R. Yeats, K. Von Dessonneck		8. CONTRACT OR GRANT NUMBER(s) DAAB07-78-C-2402
9. PERFORMING ORGANIZATION NAME AND ADDRESS Varian Associates, Inc. 611 Hansen Way Palo Alto, CA 94303		10. PROGRAM ELEMENT, PROJECT, TASK AREA & WORK UNIT NUMBERS 1L1 62701 AH92
11. CONTROLLING OFFICE NAME AND ADDRESS U.S. Army Communication R&D Command Fort Monmouth, NJ 07703 Attn: DRDCO-COM-RM-1		12. REPORT DATE 1 January 1981
		13. NUMBER OF PAGES 65
14. MONITORING AGENCY NAME & ADDRESS(*if different from Controlling Office*)		15. SECURITY CLASS. *(of this report)* Unclassified
		15a. DECLASSIFICATION/DOWNGRADING SCHEDULE

16. DISTRIBUTION STATEMENT *(of this Report)*

Approved for public release; distribution unlimited.

17. DISTRIBUTION STATEMENT *(of the abstract entered in Block 20, if different from Report)*

18. SUPPLEMENTARY NOTES

19. KEY WORDS *(Continue on reverse side if necessary and identify by block number)*

indium gallium arsenide phosphide

photodiode

indium gallium arsenide

indium phosphide

avalanche photodiode

20. ABSTRACT *(Continue on reverse side if necessary and identify by block number)*

Hybrid-structure InP-InGaAsP APDs have been fabricated which have negligible dark current ($I_D < 6$ nA at $M = 30$). The excess noise factor, F, for a hole-initiated avalanche, has been determined to be $F/M = 0.42 \pm 0.10$ for $5 \leq M \leq 35$. Conventional-structure high-bandgap (1.27 eV) InGaAsP APDs have been fabricated. These resemble low-leakage InP APDs rather than the high-leakage low-bandgap (1.00 eV) InGaAsP APDs. Low-noise bipolar transimpedance preamps have been designed and fabricated. These have bandwidths out to

DD FORM 1473 EDITION OF 1 NOV 65 IS OBSOLETE

500 MHz (for $R_f = 1$ KΩ). The sensitivity of the best hybrid APDs used with these preamps is estimated to be - 46.6 dBm for a 100 Mbit/sec, 10^{-9} bit error rate system, operating at a wavelength of 1.1 μm.

SUMMARY

Hybrid-structure InP-InGaAsP APDs have been fabricated which have negligible dark current ($I_D < 6$ nA at M = 30). The excess noise factor F, for a hole-initiated avalanche, has been determined to be F/M = 0.42 ± 0.10 for $5 \leq M \leq 35$. Conventional structure high-bandgap (1.27 eV) InGaAsP APDs have been fabricated. These resemble low-leakage InP APDs rather than the high-leakage low-bandgap (1.00 eV) InGaAsP APDs. Low-noise bipolar transimpedance preamps have been designed and fabricated. These have bandwidths out to 500 MHz (for $R_f = 1$ KΩ). The sensitivity of the best hybrid APDs used with these preamps is estimated to be − 46.6 dBm for a 100 Mbit/sec, 10^{-9} bit error rate system, operating at a wavelength of 1.1 μm.

PREFACE

TABLE OF CONTENTS

1. INTRODUCTION

This is the final report of this program and also covers in detail developments during the last 10 months. The program has been aimed at developing high-performance APDs[1-15] and preamps for optical fiber communication in the 1.0-1.3 μm spectral range. In previous reports for this program,[12-14] we have indicated that conventional-structure InGaAsP/ InP APDs have an apparently insurmountable leakage current problem when biased near breakdown. We have demonstrated by a variety of experiments[3,4,13,14] that the excess leakage current is a uniform bulk property, not associated with microplasmas or surface leakage.[4] There is recent work that suggests tunneling is responsible for this excess leakage current.[10]

In recent work, the leakage current problem in InGaAsP has reportedly been side-stepped by fabrication of hybrid InP-InGaAsP APD structures.[6,7,15] Such structures have an InP avalanche region and a separate InGaAsP absorbing region. We have fabricated a variety of hybrid InP-InGaAsP APD structures and these will be discussed in this report. The best of these hybrid APDs have negligible dark current ($I_D < 6$ nA at $M = 30$), and an excess noise factor of $F/M = 0.42 = $ const, for $5 \le M \le 35$. Such APDs improve receiver sensitivity by 11-14 dB over comparable nonavalanching photodiodes.

In an effort to determine whether the alloy nature of InGaAsP was responsible for the excess leakage current near breakdown, we fabricated some conventional structure (i.e., nonhybrid) high-bandgap (1.27 eV) InGaAsP APDs. These were seen to resemble low-leakage InP APDs[8,9] rather than the high-leakage low-bandgap (1.00 eV) InGaAsP APDs.[1-5] Hence the bandgap seems to be more important in determining the excess leakage current than possible alloy disorder effects in InGaAsP. We discuss these high-bandgap InGaAsP APDs in this report.

1

We have designed and fabricated a variety of low-noise bipolar transimpedance amplifiers for use with our APDs. Bandwidths to 500 MHz (for $R_f = K\Omega$) have been achieved. These will be discussed in this report.

The best NEP achieved with our hybrid APDs and preamps is 2.6×10^{-13} W/$\sqrt{Hz}$ for a 50-MHz ($\approx$ 100 Mbit) system. For a 10^{-9} bit error rate (b.e.r.), the sensitivity is estimated to be -46.6 dBm at a wavelength of 1.1 μm (where the quantum efficiency was 50%).

2. CONVENTIONAL STRUCTURE HIGH BANDGAP (1.27 eV) InGaAsP APDs

It is possible that the leakage current problem in conventional InGaAsP APDs[1-5] is related to the fundamental alloy nature of these materials. To shed some light on this question, we fabricated some high-bandgap (1.27 eV) InGaAsP APDs. These APDs were found to resemble low-leakage InP APDs[8,9] rather than the higher-leakage lower-bandgap (1.00 eV) InGaAsP APDs.[1-5] Hence, alloying, per se, does not cause the excessive leakage current near breakdown in the lower-bandgap InGaAsP APDs. We will now report, in some detail, on these high-bandgap APDs.

The structure of the 1.27-eV APDs is shown schematically in Fig. 1 (not to scale). The (100)-oriented InGaAsP layer was grown by LPE at a constant growth temperature of 640°C from a melt supercooled by 10°C. After growth, a drive-in diffusion was performed to move the p-n junction 1.1 μm into the InGaAsP layer from the Zn-doped ($1 \times 10^{18} cm^{-3}$) substrate. The remaining n-type part of the InGaAsP layer is 3.3 μm thick. The area of these APDs is ~3×10^{-4} cm^2 and the breakdown voltage is about 53V.

Up to gains of about M = 20, these APDs had very low dark current. The lowest dark current (I_D) at M = 20 was seen to be 50 nA, indicating a premultiplication dark current of only I_D/M = 2.5 nA (assuming all the leakage current is multiplied). This compares to I_D/M ~1 nA for typical InP APDs[8,9] having the same area. The gain and premultiplication dark current as functions of voltage for a typical APD are shown in Fig. 2. The gains were measured at 4 MHz by modulating a GaAs LED. The dark current at low voltage had considerable variation between diodes, indicating that a major fraction is defect related. Gains greater than 300 were seen for these diodes. However, near M = 20, very sharp microplasmas set in, as indicated by a sudden very sharp increase in leakage current and noise. Because of the extra noise, gains near 300 could
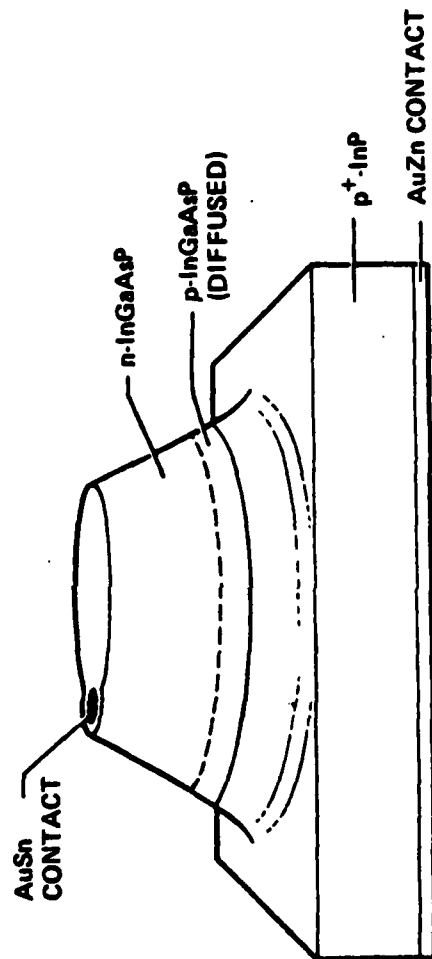
AuSn CONTACT

n-InGaAsP

p-InGaAsP
(DIFFUSED)

p⁺-InP

AuZn CONTACT

Fig. 1   1.27-eV bandgap InGaAsP APD structure.

4
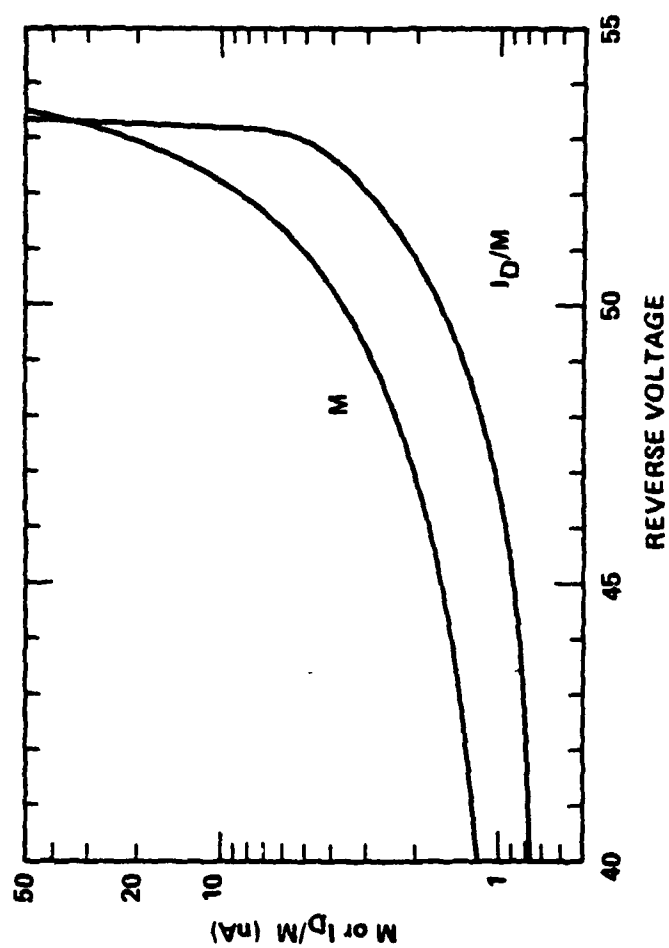
Fig. 2   Dependence of gain (M) and dark current (I_D) on voltage.

only be seen in narrow bandwidths at low frequencies. Gain uniformity scans indicated only minor gain variations, and light emission (described below) occurred in a uniform glow rather than in discrete spots, thus indicating the optically-sensitive area was free of microplasmas. We suspect the microplasmas lie underneath the electrical contact pad and are caused by damage in the underlying layer induced by contact formation. The point to emphasize, however, is that 1.27-eV InGaAsP APDs, prior to the onset of microplasmas, have very low leakage currents and are similar to InP APDs. Gains considerably greater than 20 with low dark currents may be expected when the microplasma problem is reduced. Figure 2 shows that even prior to the onset of microplasmas, the dark current increased faster than the gain ($I_D \propto M^{1.7}$). Similar behavior occurs for the 1.00-eV InGaAsP APDs and is thought to be due to a uniform bulk property,[4] possible tunneling.[10]

To obtain the lowest noise APD, the avalanche must be initiated by the carrier with the highest ionization coefficient. Noise measurements were used to determine the excess noise factor, F, which is related to the electron (α) and hole (β) ionization coefficients by[11]

$$F = M\left[1 - (1 - K)\left(\frac{M-1}{M}\right)^2\right] \xrightarrow[M \gg 1/K]{} KM \quad , \tag{2.1}$$

where $K = \beta/\alpha$ if electrons initiate the avalanche or $K = \alpha/\beta$ if holes initiate the avalanche. More exactly, in the case where K is not independent of electric field, K represents a suitably averaged ratio of ionization coefficients.[11] The rms APD noise current, I_n (in Amps), is related to F and the average primary photocurrent, I_o, by

$$I_n^2 = 2q B I_o M^2 F \tag{2.2}$$

where B is the _noise_ bandwidth of the measurement system. To determine F, I_n was amplified by a low-noise broadband amplifier having corner

6

frequencies of 2 MHz and 50 MHz, and an equivalent input noise current of 3×10^{-8}A. The amplified noise signal was sensed in a power meter. Calibration of the measurement system was provided by biasing the APD to only 40% of the breakdown voltage (where M = F = 1), and measuring the shot noise of a large (~80 μA) DC photocurrent. (It was verified that I_n^2 was linear with I_o, as Eq. (2.2) demands.) This calibration procedure for determining I_n^2 agreed within experimental uncertainties (~30%) of a calibration based on the approximately-known amplifier gain and frequency response. (See Sec. 3.1 for a more complete discussion of this procedure.) Noise measurements were taken for the diode of Fig. 2. A GaAs LED was used to generate a primary photocurrent of 47 nA. The rapid optical absorption near the surface of the 1.27-eV APD insured that the avalanche was initiated only by holes. We found F/M = 1.0 ± 0.2 for all M between 5 and 23. By Eq. (1), we estimate β/α = 1.1 ± 0.4.

The 1.27-eV APDs were examined for light emission using an infrared microscope with S-1 response and about 2-μm resolution. At a few milliamps of reverse current, the 1.27-eV APDs began to glow dimly and uniformly. There were no bright spots, which indicates that the (unshaded) photosensitive area was free of microplasmas or edge breakdown. We can see such bright spots in some InP APDs. Hence we believe that any microplasmas present had to be underneath the contact pad. The magnitude of the avalanche-generated light was estimated by using a 12-mil diameter $In_{.53}Ga_{.47}As$ detector (E_g = 0.75 eV), located 50 mils away from the 1.27-eV APD. Due to the strong absorption of above-bandgap light, most of the detected light is in the 0.75 to 1.27-eV range. The light generated was linearly proportional to the APD bias current for all bias currents examined (between 10 μA and 5 mA). Photocurrent sensitivity was about 1 pA. Assuming that the APD is a (two-sided) Lambertian emitter, and estimating the average quantum efficiency of the detector to be 0.5, we estimate that the total external quantum efficiency for photon creation in the range between 0.75 eV and 1.27 eV is 6×10^{-5}.

Similar measurements have been made on our conventional-structure
(Ref. 13, p. 6) 1.00-eV bandgap InGaAsP APDs, with the result that the
external quantum efficiency for photon generation between 0.75 eV and
1.00 eV is about 3×10^{-5} in most diodes examined. The average external
quantum efficiency _per unit energy_ is thus nearly the same for both the
1.00-eV APDs and the 1.27-eV APDs, having the value 1×10^{-4}/eV. With
such similar light emission, one is tempted to infer that the 1.00-eV
APDs have uniform light emission, since the 1.27-eV APDs do. (Only the
1.27-eV light can be seen by an infrared microscope with S-1 response.)
This would be another indication that the breakdown in good 1.00-eV APDs
is uniform and not caused by microplasmas. The excess leakage current
near breakdown in the 1.00-eV APDs could well be associated with tunnel-
ing.[10]

3. HYBRID STRUCTURE InP-InGaAsP APDs

In February of 1979, we first fabricated hybrid structure APDs[16] --
i.e., APDs having an InP avalanche region and a separate InGaAsP absorbing
region. These APDs unfortunately had microplasma breakdown occur as
soon as the depletion region reached the InP-InGaAsP interface. Further
efforts at such structures were not made until about 6 months later,
when NEC reported[6,7] hybrid structure InP-InGaAsP APDs that seemed to
work -- i.e., avalanche gain occurred with reduced leakage current.
Since that time, we have fabricated a variety of successful hybrid APD
structures.

We fabricated the NEC planar hybrid APD structure[6,7] on two wafers.
The structure is shown in Fig. 3. Device performance results were ambi-
guous. The I-V characteristics were rather "loopy" (at 60 Hz) near
breakdown, which is indicative of charge storage either at an external
surface or at the InP-InGaAsP interface. There was also some peculiar
frequency dependence to the gain. When the curve-tracer was swept at 60
Hz, substantially larger gains occurred than when the diodes were DC
biased. For example, one diode with the voltage swept at 60 Hz had $M = 20$ at a (multiplied) dark current of $I_D = 5$ µA. (The APD diameter is 8
mils.) Another diode had $M = 400$ at $I_D = 200$ µA under AC conditions,
but only $M = 25$ at $I_D = 200$ µA when DC biased. We do not understand
this behavior. It may well be anomalous (and hard to reproduce). In
any case, this structure is not the preferred one. One problem with
this structure is that premature breakdown can occur at the edges of the
active region under certain conditions of doping or junction curvature.
The inverted mesa structures discussed below do not have this problem.

Two types of hybrid APD inverted-mesa structures were fabricated.
The first type is preferred if $\beta > \alpha$, while the second type is preferred
if $\alpha \gtrsim \beta$. (α and β are the electron and hole ionization coefficients,

p$^+$-InP
(Zn-diffused)

AuZn

SiO$_2$

n-InP

n-InGaAsP

n$^+$-InP
(substrate)

AuSn

6.0 μm

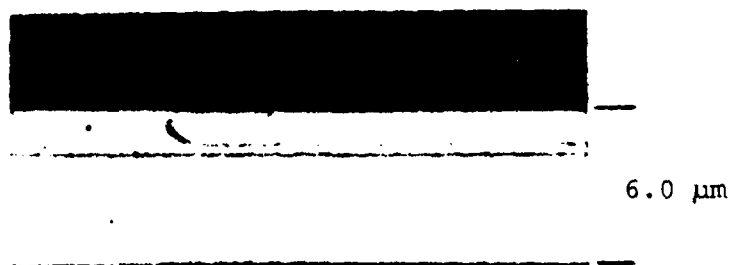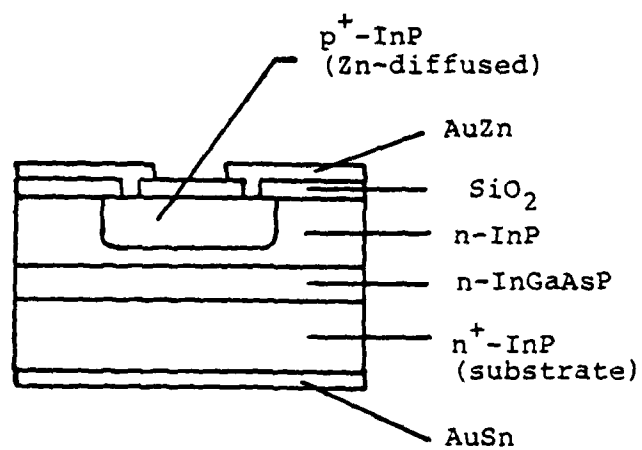Fig. 3   Planar hybrid APD structure.

respectively.) We have recently determined that Type I structures have $\beta > \alpha$, so that the preferred structure is the Type I structure which we now discuss.

3.1 Type I Hybrid APDs

The characteristics of a Type I APD are summarized in Fig. 4. The Type I structure (Fig. 5) is grown by liquid phase epitaxy (LPE) and consists of p^+-InP(substrate)/p-InP(diffused)/n-InP/n-InGaAsP. The p-InP region is formed by diffusing Zn from the substrate into an n-InP epilayer, thereby leaving an n-InP region of the desired thickness (~1.4 µm). This structure is designed to be illuminated through the substrate for optimum speed and quantum efficiency. When the APD is biased near breakdown, the depletion region (~1.5-2.0 µm wide) must just barely extend into the top InGaAsP layer. The depletion region must not extend very far into the InGaAsP layer in order that the electric field be kept well below the breakdown field. High electric fields in InGaAsP cause the large excess leakage current near breakdown found in conventional (nonhybrid) ~1.0 eV InGaAsP APDs. Hence the thickness of the n-InP region of Fig. 5 is critical. The fabrication approach used was to calibrate the drive-in diffusion process with a small test piece from the given wafer, and then to divide the wafer up into 2 or 3 pieces so that 2 or 3 nearby values of d would result from 2 or 3 slightly different drive-in diffusions. In spite of this "shot gun" approach, most wafers had poor APDs. The best piece of the best wafer had a low yield of good APDs. A few of these were outstanding. Only one of these outstanding APDs, however, made it completely through packaging and testing so that it could be included in the hardware shipment of this contract. With more experience, the low-yield problem may be solved, although fabrication will still be difficult (due to the precision needed during the drive-in diffusion step). The low yield might possibly be associated with nonuniform diffusion from the substrate, since occasionally dips in the diffusion front could be seen. Perhaps use of substrates from a variety of bulk crystals would be helpful in future work.

Optimum Gain: M_{opt} = 24 for 10^{-9} b.e.r., 100 Mbit/sec system

Dark Current: I_D < 6 nA at M = 30

Maximum Gain Nonuniformity at <M> = 25: +22%

Excess Noise Factor, F: F/M = 0.42 ± 0.10 for $5 \leq M \leq 35$

Breakdown Voltage: $V_{BD} \approx$ 75 V

Diameter: 150 microns

Capacitance: 1.0 pF

Spectral Response: 0.97 - 1.24 μm

Quantum Efficiency: 50%

Rise Time: < 0.5 nsec

Fall Time: 3 nsec

Fig. 4   Type I hybrid InP-InGaAsP APD specifications.

The better of these Type I APDs have a reverse I-V characteristic similar to that shown in Fig. 6. (This figure is for the Type I diode that has been delivered.) At a gain of 30, the dark current is less than 6 nA. The step in photoresponse seen at ~35V occurs when the depletion region edge reaches the InGaAsP interface. For this APD, d ≈ 1.4 μm was obtained both by C-V profiling (Fig. 7) and by inspection of a cleaved and stained cross section. The breakdown voltage for the diode of Fig. 6 was ~76V and the capacitance for the 150-μm diameter APD was 1.0 pF (excluding package capacitance of 0.3 pF). The APDs are illuminated through the substrate and are packaged in sealed micro-window packages, similar to that shown in Fig. 8. Such packages allow nearly 100% coupling efficiency from optical fibers with core diameters up to 100 μm (NA < 0.30).

AuSn contact

n-InGaAsP

n-InP

p-InP
(diffused)

p+ (Zn)-InP

AuZn contact with
opening below mesa

Illumination
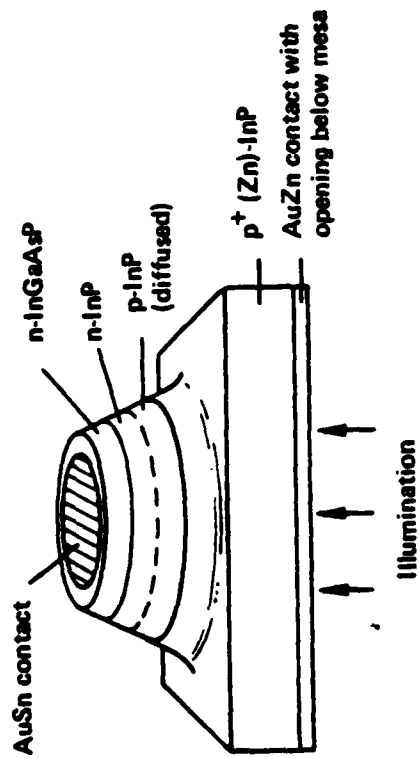
Fig. 5   Type I hybrid APD structure.

13

The key to the package is the 75-μm thick GaP window chip, upon which sits the photodiode chip. GaP is transparent (even in the visible), is as hard as quartz, has high thermal conductivity, and is resistant to most chemicals. It is electrically conductive when doped; (conductive GaP is preferred, since then the conductive epoxy shown in Fig. 8 could be eliminated). In addition, because of the high index of refraction of GaP ($n \approx 3$ in the infrared), light spreads relatively little in it compared to air or quartz; (e.g., light spreads about the same amount in 3 mils of GaP as in 1 mil of air). Hence a 3-mil GaP window introduces nearly negligible spreading: only a 10-μm increase in spot diameter results from a 0.20 NA optical fiber. Reflection losses are effectively reduced by antireflection coatings.

At a gain just over $M = 35$, a microplasma forms in the diode of Fig. 6 which causes a sudden increase in dark current, although the gain continues to increase even beyond this point. Since optimum sensitivity typically occurs for $M \leq 30$, microplasmas will generally not be a problem under normal operating conditions. The maximum gain nonuniformity at an average gain of 25 was +22%, as measured by scanning a 70-μm light spot.

The DC gain is the same as the rf gain at low light levels, and follows S. L. Miller's semi-empirical relationship[17] with an exponent n = 3.5 ± 0.3 for $M > 3$, with larger values occurring at lower gains (n ≈ 5.2 at $M = 1.3$). This compares to n ≈ 2-8 for silicon and Ge APDs. The quantum efficiency at 40V (where M=1) is 50% at 1.06 μm (as measured using a 1.06-μm LED coupled to the packaged APD by a 63-μm core 0.2 nA optical fiber); the long wavelength cutoff in spectral response is at ≈1.24 μm. The main reason the quantum efficiency is not larger at 1.06 μm is due to free carrier optical absorption in the $1 \times 10^{18} cm^{-3}$ Zn-doped

14
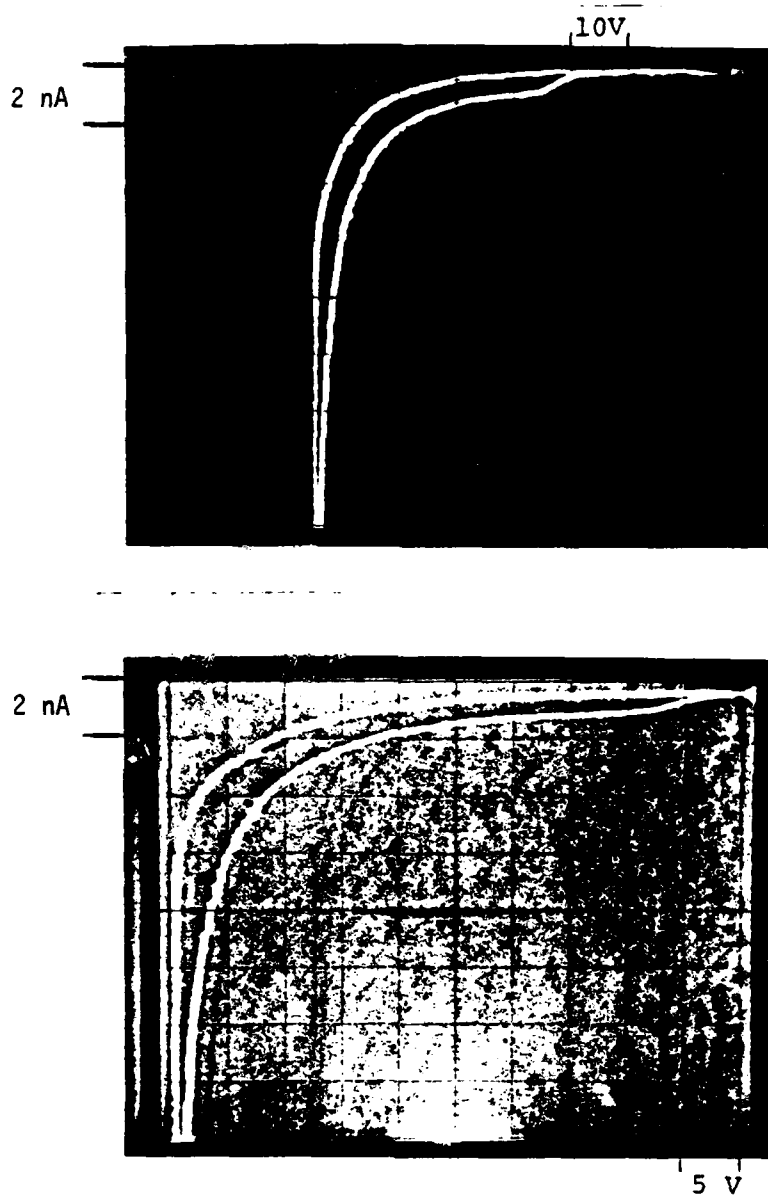
Fig. 6   Type I hybrid APD I-V characteristics:

Top: Reverse characteristics at 10V and 2 nA/div.

Bottom: Partial reverse characteristic beginning
          at ~25V at 5V and 2 nA/div.

For both photos, the upper curve is the dark current,
  while the lower curve includes a small photocurrent.
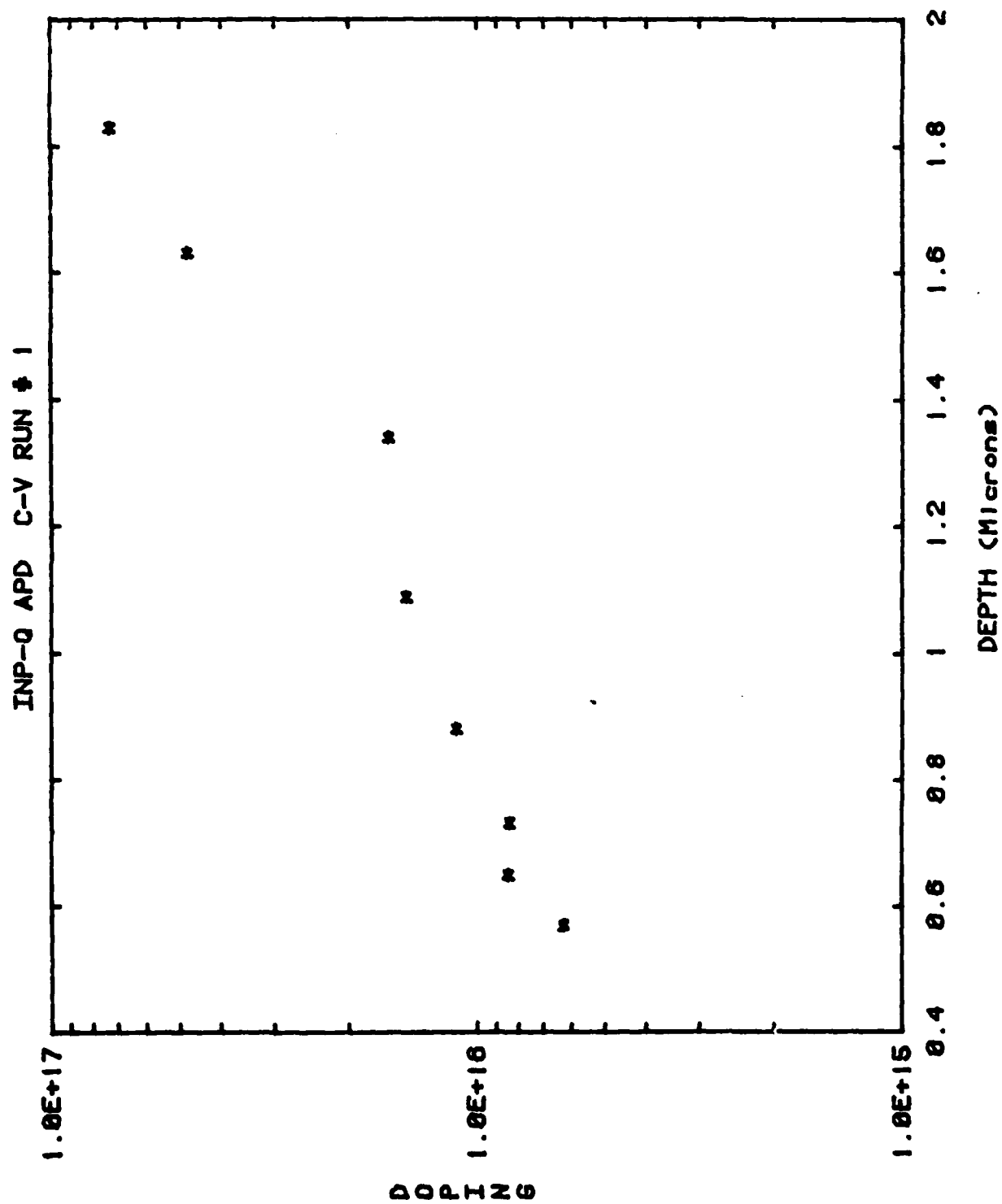
15

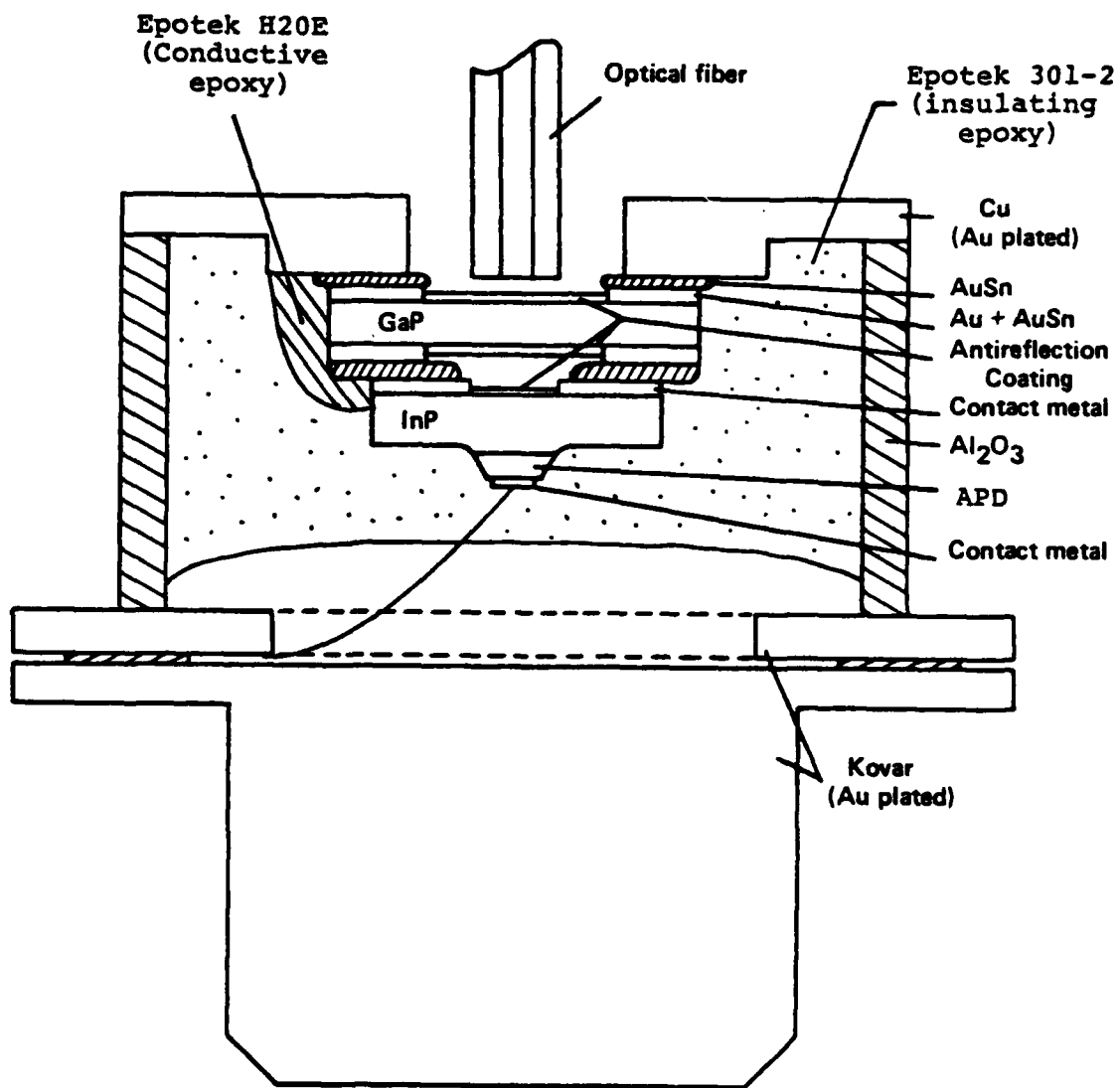Fig. 7 Doping profile of Type I hybrid APD.

Fig. 8 Micro-window APD package. The APD chip
is soldered to the special GaP window
chip, described in the text.

InP substrate (antireflection coatings have been employed). Total reflection losses of the packaged APDs are estimated to be 24% at 1.0 μm and 3% at 1.3 μm. Based on some of our recent InGaAs photodiode work[18], we estimate that free carrier absorption accounts for absorption of about 30% of the light at 1.0 μm and 40% at 1.3 μm, for a substrate 100 μm thick. Use of more lightly doped substrates ($\sim 2 \times 10^{17}$) would nearly eliminate this problem. The variation in reflection losses with wavelength cancels the variation in free carrier absorption, so that the external quantum efficiency is nearly constant ($\approx 50\%$) within the spectral response band (0.97 to 1.24 μm).

The response of the APD to a fast pulse from a 1.1-μm InGaAsP/InP laser is shown in Fig. 9. The rise time (0.8 nsec) is that of the measurement system, but the fall time is extended to ≈ 3 nsec by a diffusion tail that begins about 25% above the baseline, and which arises from holes slowly diffusing in the InGaAsP layer toward the depletion region. There was no variation of speed with gain. No such tail is seen in our high-speed $In_{.53}Ga_{.47}As/InP$ photodiodes. It is very difficult to avoid such a diffusion tail in hybrid structure APDs, since extending the depletion region substantially into the InGaAsP layer will drastically increase the leakage current. Because the diffusion tail only affects the lower part of the pulse, we find (Fig. 10) that the response time defined as the full width at half maximum (FWHM) of the response to a delta function pulse is in the subnanosecond region.

The dependence of gain and dark current near breakdown on temperature was measured using temperatures of 23°C and 44°C. The breakdown voltage V_{BD}, defined as occurring where M=15, increases with temperature according to $(\Delta V_{BD}/V_{BD})/\Delta T = 1.0 \times 10^{-3}/°C$. At the voltage where M = 15 at 23°C, M decreases by a factor of 2 for every 18°C rise in temperature. At the voltage (near breakdown) where the 23°C dark current is 6 nA, the dark current approximately doubles every 15°C.
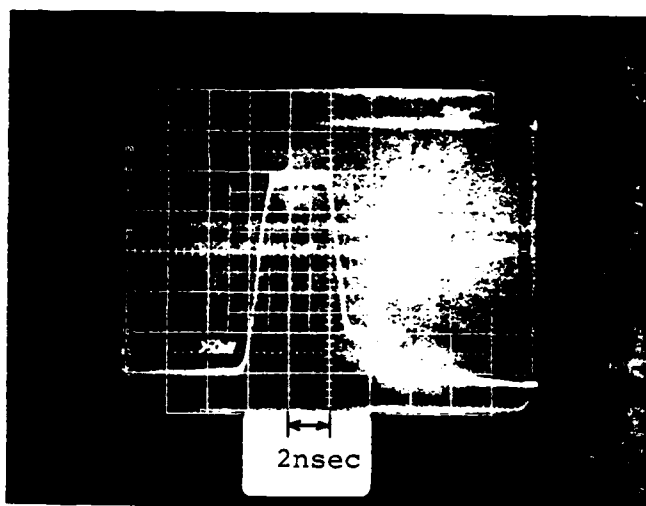
2nsec

Fig. 9 Response of Type I APD to fast rectangular
pulse from 1.1-um InGaAsP/InP laser. The
rise time (0.8 nsec) is that of the measure-
ment system. A diffusion tail extends the
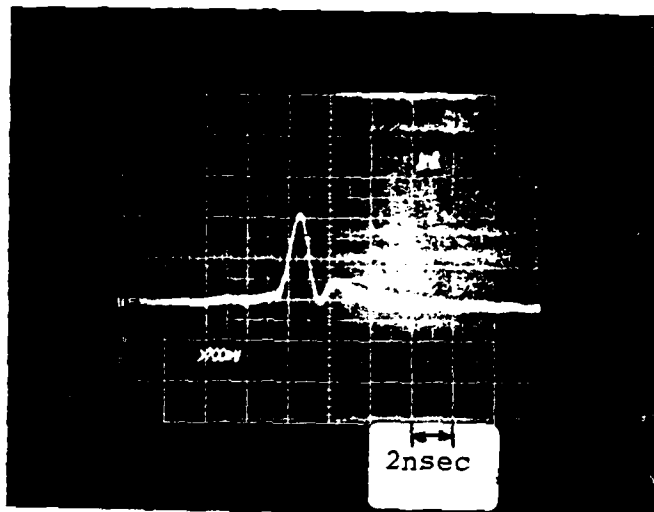fall time to ≈ 3 nsec.

Fig. 10   Impulse response of Type I APD.   FWHM of
          measurement system is 0.8 nsec.

Careful noise measurements were made to determine the excess noise factor, F. For illumination through the substrate, the avalanche is initiated by holes, and we found $F/M = 0.42$. F/M was constant for $5 \leq M \leq 35$ to within $\pm 10\%$. There may also be systematic errors in F/M totaling $\pm 20\%$; these arise mainly from assuming that the quantum efficiency is constant above 40V and that $M=1.00$ at 40V. Actual measurement and calibration accuracy is $\pm 5\%$.

Use of the shot noise of a large photocurrent at 40V to calibrate the noise measurements allows F/M to be obtained using only relative (not absolute) power measurements, and does not require knowledge of amplifier gain or frequency response. Let $I_{PH,0}$ be a large DC photocurrent (~50 µA) at low bias (~40V) where $M = 1$, whose shot noise generates a noise power reading of $P_{D,0 + PH,0}$ (after several steps of AC-coupled amplification). Let $P_{D,0}$ be the corresponding power reading in the dark. Next, bias the APD near breakdown and measure the gain and multiplied DC photocurrent, I_{PH} of a <u>small</u> primary photocurrent. A <u>small</u> primary photocurrent must be used so that gain saturation is not occurring; the rf gain should then be the same as the DC gain (this was confirmed to be the case). I_{PH} generates a power reading of P_{D+PH}. Let P_D be the corresponding power reading in the dark; ($P_D = P_{D,0}$ if there is negligible dark current). If one makes the usual assumption that noise power adds algebraically, then one can show that the excess noise factor is given by

$$F = \frac{\dfrac{I_{PH,0}/I_{PH}}{M}\left[\dfrac{P_{D+PH}}{P_{D,0}} - \dfrac{P_D}{P_{D,0}}\right]}{\left[\dfrac{P_{D,0+PH,0}}{P_{D,0}} - 1\right]} \tag{3.1}$$

21

The advantage of this procedure is that only relative power measurements are needed, and that amplifier gain and frequency response need not be known. This is particularly helpful in broadband measurements, since the noise bandwidth is often difficult to determine precisely, but need not be known when using the above technique.

The simple form $F/M = const \equiv K$, ($K = 0.42$) allows simple analytic expressions describing APD performance to be obtained (Appendix A). For a given signal-to-noise ratio (SNR) of electrical power, the optimum sensitivity (if there are no microplasmas) occurs at a gain of

$$M_{opt} = (3\ SNR)^{-1/4}\ (I_n/qBK)^{1/2} \tag{3.2}$$

and the required optical power is

$$P_R = \left(\frac{h\nu}{\eta q}\right) (3\ SNR)^{3/4}\ (q\ B\ K\ I_n)^{1/2} \quad . \tag{3.3}$$

At optimum or nonoptimum M, the noise equivalent power (NEP) is given by

$$NEP = \frac{h\nu}{\eta q} \left\{ qMK\ \sqrt{B} + \sqrt{q^2 M^2 K^2 B + I_n^2/(M^2 B)} \right\} \quad . \tag{3.4a}$$

$$M \ll M_{opt} \quad \frac{h\nu}{\eta q M}\ \frac{I_n}{\sqrt{B}} \tag{3.4b}$$

Here, B is the noise bandwidth in Hz, I_n is the equivalent rms input noise current of the preamp (in amps) and η is the quantum efficiency for a photon having energy of $h\nu$. We have assumed that the shot noise of the dark current is small compared to I_n. This is true for the APD of Fig. 5 up to gains over 30. With $B = 50$ MHz and $I_n/\sqrt{B} = 3.6$ pA/$\sqrt{Hz}$ (as for our preamps, see Sec. 4.2), and with SNR = 36 (as for a 10^{-9} b.e.r.),

22

one finds by Eq. (3.2)

$$M_{opt} = 27 \qquad\qquad (3.5)$$

The required optical power at $\lambda = 1.1$ μm and $\eta = 50\%$ for the Type I
APD is then

$$P_R = 2.2 \text{ nW} = -46.6 \text{ dBm} \qquad\qquad (3.6)$$

This is slightly better than the sensitivity that a state-of-the-art
pin-FET module could achieve,[19,20] but there are no problems with
dynamic range and no need for equalization.

We have observed that at high gains microplasma pulses occasionally
form, even before the DC photocurrent begins its sharp increase at $M \approx$
35. These may be rare enough at M = 30 so that they do not noticeably
contribute to the average noise. However, they do affect the bit error
rate. Operation at slightly lower gains is preferred in order to reduce
or eliminate the occurrence of these microplasma spikes. At M = 24, the
microplasma spikes occur minutes apart and have subnanosecond pulse
widths; hence at M = 24, the spikes would have little effect on the
error rate of a 50-Mbit 10^{-9} b.e.r. system. Similar behavior occurs for
silicon APDs operated at high gains.

3.2 Type II Hybrid InP-InGaAsP APDs

Another type of hybrid APD structure that we have fabricated is
shown in Fig. 11. This Type II APD structure consists of p^{+}-InP(sub-
strate)/ p-InGaAsP(diffused)/p-InP(diffused)/n-InP. To obtain this
structure, we first grow (by LPE) the structure p^{+}-InP(substrate)/n-
InGaAsP/n-InP; we then perform a deep drive-in diffusion of Zn from the
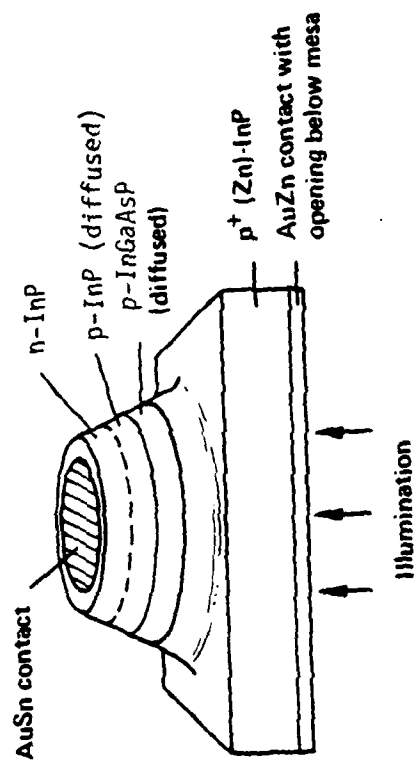substrate, so that the p-n junction is located in the top InP layer

23

AuSn contact

n-InP
p-InP (diffused)
p-InGaAsP (diffused)

p+ (Zn)-InP
AuZn contact with opening below mesa

Illumination

Fig. 11   Type II hybrid APD structure.

24

slightly above ($\leq$ 1.0 µm) the InGaAsP layer. The junction is quite graded so that the depletion region extends (downwards) into the InGaAsP layer at low biases. The substrate is Zn doped (1 x 10^{18}cm^{-3}), while the n-layers are unintentionally doped at about 2 x 10^{16}cm^{-3}.

We have fabricated Type II APDs using InGaAsP layers having bandgaps of either 1.31 µm or 1.24 µm. The 1.24-µm structure is easy to grow. However, to obtain spectral response out to 1.3 µm, we are more inter- ested in the 1.31-µm structure. The 1.31-µm structure is much harder to grow by LPE, partly because 1.31-µm layers are harder to reproducibly grow than 1.24-µm layers, but mostly because the melt for the top InP layer tends to partially dissolve the underlying quaternary layer when its bandgap is 1.31 µm (but not 1.24 µm). A variety of growth condi- tions have been used, including up to 15°C of supercooling. Even on the best wafers, only part of the wafer is free from meltback. An example of partial dissolution of a 1.31-µm layer is shown in Fig. 12.

The I-V characteristic of a typical 1.31-µm Type II APD is shown in Fig. 13. The step in photoresponse at ~5V occurs when the depletion region reaches the InGaAsP layer. The doping profile, obtained by C-V measurements, is shown in Fig. 14. Note that the junction is graded near the center of the junction. A cleaved and etched sample indicated that the p-n junction was located 1.0 µm above the InGaAsP layer, which is consistent with the I-V and C-V data. There is usually a high yield of low-leakage Type II APDs with gain (on a good wafer), but the maximum gain obtained before microplasma formation has so far been rather small.

We have fabricated 1.24-µm Type II APDs with gains up to M = 9 with dark current of I_D = 100 nA; (diode area is 3 x 10^{-4}cm^2; breakdown voltage is $\approx$ 82V). Most diodes have gains of only 3-5 before micro- plasmas form, resulting in a sudden increase in leakage current and noise. However, these initial 1.24-µm Type II APDs were not optimum, since the p-n junction was just barely ($\approx$0.3 µm) inside the top InP layer.
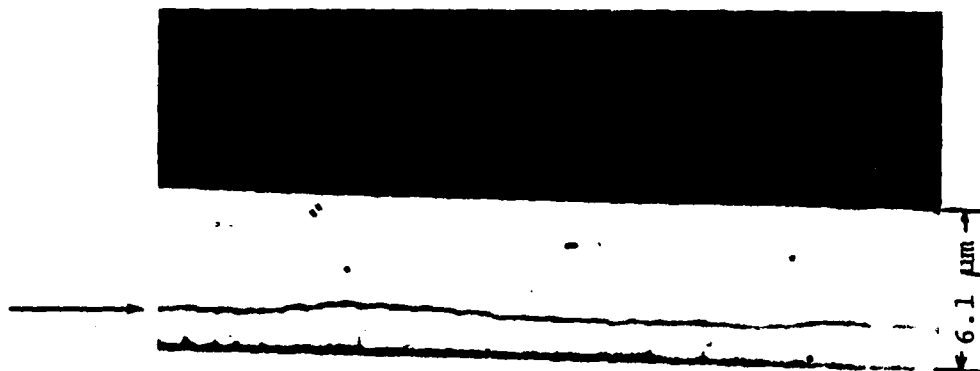
25

Fig. 12   Partial dissolution of a 1.31-μm bandgap InGaAsP
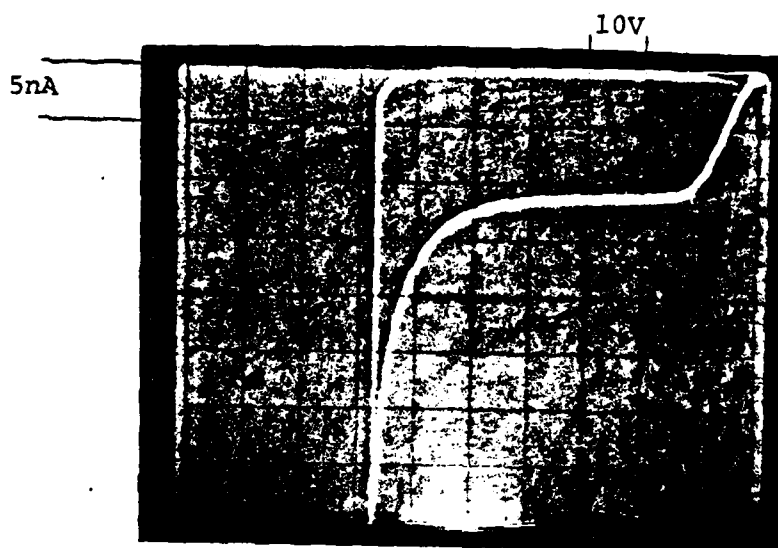   layer by an InP melt supercooled by 15°C.

Fig. 13   Type II hybrid APD reverse I-V characteristic.
The upper curve is the dark current, while the
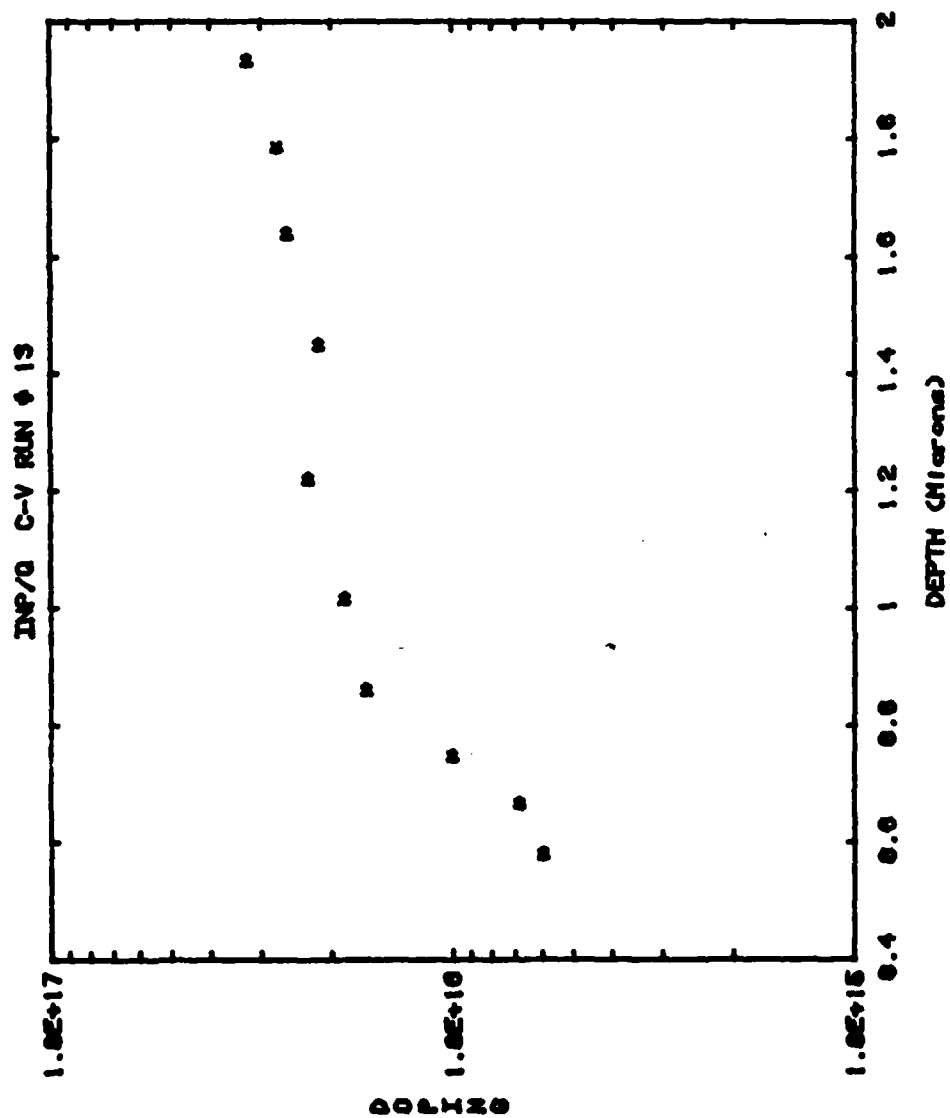lower curve includes a small photocurrent.

27

Fig. 14   Doping profile of Type II hybrid APD.

The 1.31-μm Type II APDs have the p-n junction about 1.0 μm into the top layer, but still tend to form microplasmas at low gains. Maximum gain prior to microplasma formation is M = 5, with M = 3-4 being typical. Prior to microplasma formation, these 150-μm diameter APDs have dark currents of only a few nanoamps, typically, and the gain is quite uniform. As with the Type I APDs described earlier, the Type II APDs need to be operated at gains slightly below the point where the dark current increases sharply in order to avoid occasional microplasma spikes. Hence M = 3 is typically a good operating point. At such low gains, the gain process is essentially noiseless for (the small) signals of interest. Hence, the ratio of electron (α) and hole (β) ionization coefficients is not very important -- e.g., M = 3 improves the sensitivity by a factor of 3. However, if large useful gains become available, the excess noise factor and the ratio of ionization coefficients will become important. For the 1.24-μm Type II APDs described above, we measured the excess noise factor, F. For M near 5, we found F/M = 1.3 ± 0.2 for an electron-initiated avalanche. This excess noise factor implies β/α = 1.5 ± 0.3. For the 1.24-μm Type II APDs whose noise properties were measured, the InGaAsP layer probably was an active part of the avalanche process, since the p-n junction was only ~0.3 μm into the InP layer. Hence the excess noise factor that was measured may be a characteristic of InP _and_ InGaAsP, not simply InP.

Type II APDs may be illuminated from either the top side or through the substrate without a big difference in the quantum efficiency or speed, so long as the InGaAsP layer is not too thick (≤2.0 μm). For thicker InGaAsP layers, top-side illumination would be preferred. Top-side illumination would also be preferred for improved quantum efficiency if free carrier absorption in the substrate is important. The Type II APDs delivered under this contract had a bandgap of 1.31 μm and were packaged for illumination through the substrate. Quantum efficiency was measured at 1.06 μm using an LED coupled to the packaged APD with a

63-μm core, 0.21 nA optical fiber. At 30V, the quantum efficiency was 40%. Quantum efficiency is nearly constant within the spectral response band of 0.97-1.31 μm, just as for the Type I APDs. Again, 30-40% of the light is lost to free carrier absorption in the p^+-InP substrate. For these particular APDs, the InGaAsP layer was only about 0.8-μm thick. This allows about 20% of the light to pass through the layer without being absorbed. More lightly doped substrates and slightly thicker InGaAsP layers are desirable, in order to raise the quantum efficiency above 80%.

The response of a 1.31-μm Type II APD to a fast pulse from a 1.1-μm InGaAsP laser is shown in Fig. 15. The rise and fall times (0.8 nsec) are those of the measurement system. Actual rise and fall times are < 0.5 nsec. There is no variation of speed with gain. Type II APDs are faster than Type I APDs because photoelectrons (Type II) diffuse faster than photoholes (Type I). In particular, the fall time of a Type II APD that is associated with a diffusion tail would be smaller than that for a Type I APD by the mobility ratio μ_e/μ_h -- a factor of ~40.

The properties of all the hybrid APDs delivered to the Army under this contract are summarized in Fig. 16. APD #1 is Type I; the remaining APDs are Type II.
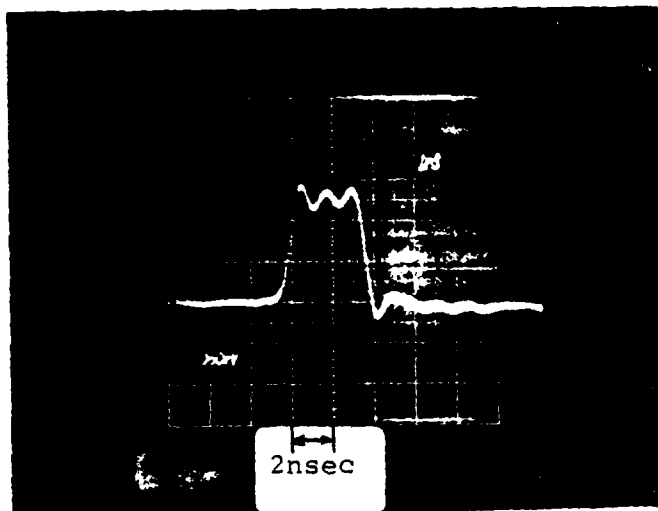
2nsec

Fig. 15 Response of Type II APD to fast pulse from 1.1-μm
         InGaAsP/InP laser. The rise time and fall time
         are those of the measurement system (0.8 nsec).

31

Fig. 16 Summary of Varian APD characteristics.

APD No.	1) V_{OPT} (V) (optimum bias voltage)	M_{OPT} (gain at V_{OPT})	I_D (nA) (dark current) at V_{OPT}	2) C (pF) (at V_{OPT})	3) Spectral bandwidth (μm)	4) Quantum efficiency (%)	Rise time (nsec)	Fall time (nsec)
1	75.6	24.	6	1.3	0.97 – 1.24	50.4	< 0.8	3
2	65.4	2.8	5	1.3	0.97 – 1.31	40	< 0.5	< 0.5
3	67.1	3.3	9	1.3	0.97 – 1.31	40	< 0.5	< 0.5
4	62.9	3.0	5	1.3	0.97 – 1.31	40	< 0.5	< 0.5
5	61.1	2.9	5	1.3	0.97 – 1.31	40	< 0.5	< 0.5
6	66.7	2.9	3	1.3	0.97 – 1.31	40	< 0.5	< 0.5
7	67.6	3.1	9	1.3	0.97 – 1.31	40	< 0.5	< 0.5
8	67.3	2.6	4	1.3	0.97 – 1.31	40	< 0.5	< 0.5
9	68.3	3.0	2	1.3	0.97 – 1.31	40	< 0.5	< 0.5
10	66.8	3.2	4	1.3	0.97 – 1.31	40	< 0.5	< 0.5
11	67.1	3.0	15	1.3	0.97 – 1.31	40	< 0.5	< 0.5
12	60.7	2.6	7	1.3	0.97 – 1.31	40	< 0.5	< 0.5
13	67.7	2.9	3	1.3	0.97 – 1.31	40	< 0.5	< 0.5

Notes:

1) Optimization is for greatest sensitivity at low bit error rates. T = 25°C is assumed throughout.

2) Includes package capacitance of 0.3 pF. APD diameter is 150 μm.

3) These APDs are illuminated through the InP substrate and thus have a sharp short wavelength cutoff at 0.96 μm.

4) As measured from 63-μm core, 0.21 NA optical fiber, using a 1.06-μm LED. Quantum efficiency is nearly constant within the indicated spectral bandwidth. Fiber coupling loss is nearly zero for fibers with core diameters up to 100 μm (NA ≤ 0.30). Quantum efficiencies less than 100% occur mainly due to free carrier absorption in the InP substrate of the APD.

4. APD/PREAMP MODULE DESIGN

It is necessary to have a good low-noise preamp to use with APDs in order to obtain greatest receiver sensitivity. We restricted our design considerations to bipolar preamps in order to give a higher priority to the development of hybrid APDs. Bipolar preamps are more sensitive than GaAs FET front-end preamps when the capacitance to ground at the preamp input is large ($\gtrsim$ 5 pF); FET preamps are more sensitive when this capacitance is small ($\lesssim$ 5 pF). Two types of bipolar transimpedance amplifiers were investigated and will be discussed below.

4.1 Preamp Circuit Analysis

4.1.1 Analysis of a General Transimpedance Amplifier

A general transimpedance amplifier is shown in Fig. 17. The basic open-loop amplifier (obtained by setting $Z_F \to \infty$, $Z_L \to \infty$) has a (complex) voltage gain of $-G$. Symbols are defined in Fig. 17 and the Fig. 17 caption. Analysis of this circuit shows that

$$V_L = \frac{- I_s Z_f \left(1 - \frac{Z_2}{G Z_f}\right)}{1 + \frac{Z_2 + Z_L}{G Z_L}\left(1 + \frac{Z_f}{Z_1}\right) + \frac{Z_2}{Z_L}G} \qquad (4.1)$$

Normally, Z_f, Z_2, and Z_L are approximately real, having values R_f, R_2, and R_L, respectively. Also, we generally have $R_2 << |G Z_1|$ and $R_2 << |R_f|$. Equation (4.1) then becomes

$$V_L = \frac{- I_s R_f}{1 + \frac{R_2 + R_L}{G R_L}\left(1 + \frac{R_f}{Z_1}\right)} \qquad (4.2)$$

The input impedance of the transimpedance amplifier is
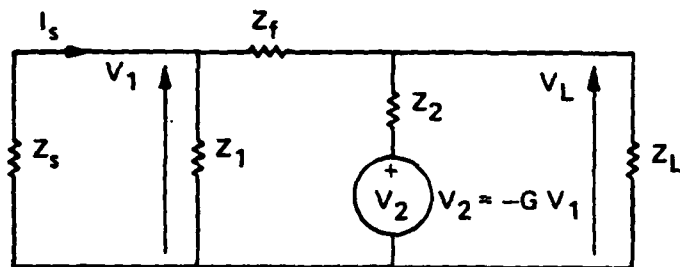
Fig. 17   Generalized transimpedance amplifier.
           Z_f is the complex feedback impedance.
           Z_S, Z_1, Z_2 and Z_L are the complex
           source, input, output, and load impe-
           dances, respectively, when $Z_f \to \infty$.
           G is the negative of the complex
           voltage gain (V_L/V_1) for $Z_f \to \infty$ and
           $Z_L \to \infty$. I_S is the current coming
           from the source.

34

$$Z_{in} \approx \frac{R_f}{G}\left(\frac{R_2 + R_L}{R_L}\right) \quad , \tag{4.3}$$

and the output impedance is roughly given by

$$Z_{out} \sim \frac{2R_2}{G} \sim 1\,\Omega \quad . \tag{4.4}$$

4.1.2 Analysis of Two-Transistor Bipolar Transimpedance Amplifier

A simple transimpedance amplifier is shown in Fig. 18. It consists of an open-loop voltage amplifier having high input impedance and low output impedance. There are two bipolar transistors in the amplifier: an input transistor in the common emitter configuration to provide voltage gain, and an output transistor in the emitter-follower configuration to provide low output impedance. The feedback resistor, R_f, that connects the output to the input results in a closed-loop amplifier with low input and output impedance.

To analyze the circuit of Fig. 18, a high-frequency model of a transistor is needed. We begin with the model discussed by J. Carroll[21] and shown in Fig. 19a. In the presence of a load Z_{L1}, this model can be reduced to the model of Fig. 19b. From Fig. 19b, the input impedance os the transistor, neglecting R_b, is

$$Z_1 \equiv \frac{\vec{\beta}\,R_e}{1 + \dfrac{Z_{L1}}{Z_0 + Z_{L1}}} \xrightarrow{\;|Z_{L1}|>>|Z_0|\;} \vec{\beta}\,R_e/2 \quad . \tag{4.5}$$

The output im

The output impedance (without the load) is

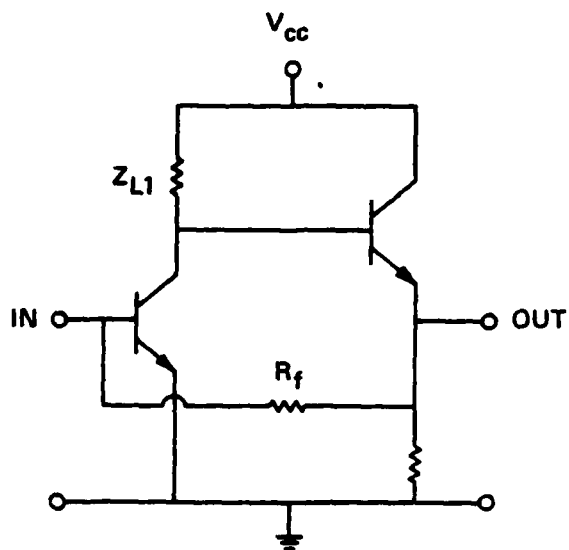$$Z_0 = \frac{1}{j\,\omega\,\vec{\beta}\,C_c} \tag{4.6}$$

Fig. 18   Simple bipolar transimpedance amplifier.

and the complex voltage gain is

$$- \vec{G} = \frac{V_c}{V_b} = \frac{- Z_{L1} || Z_0}{R_e} \qquad . \tag{4.7}$$

Here R_e ($= 1/g_m$) is the dynamic resistance of the emitter-base junction, $\omega_t/2\pi$ is the cutoff frequency of the transistor, C_c is the collector-base capacitance, and $\vec{\beta}$ is the complex frequency dependent current gain of a common emitter transistor, and is given by

$$\vec{\beta} = \beta_0/[1 + j\omega\beta_0/\omega_t] \qquad . \tag{4.8}$$

The complex Miller feedback capacitance, $- \vec{G}C_c$, has been included in these calculations. Its effect is only to introduce the factor of 2 on the right side of Eq. (4.5). The Miller effect is minimal because there is only limited voltage gain available at moderate frequencies due to a reduced ouptut impedance ($|Z_0|\sim900\Omega$ at 100 MHz).

The model of Fig. 19b can be used to show that the output impedance of an emitter follower transistor at most frequencies of interest is approximately

$$R_2 \approx R_{e2} \tag{4.9}$$

where R_{e2} is the dynamic resistance of the emitter-base junction. Equations (4.5)-(4.9) can be used with Eq. (4.2) to show that

$$V_L = \frac{- I_s R_f}{1 + j\omega C_c \left(\frac{R_{e2} + R_L}{R_L}\right)(\vec{\beta} R_e + 2R_f)} \tag{4.10}$$

Here we have comfortably assumed $R_{e2} \ll |\vec{G}\vec{\beta}R_e/2|$, $R_{e2} \ll |GR_f|$, $R_e \ll |Z_{L1}|$, and $2R_f \ll |\vec{\beta}Z_{L1}|$. Equation (4.10) shows that highest response speed
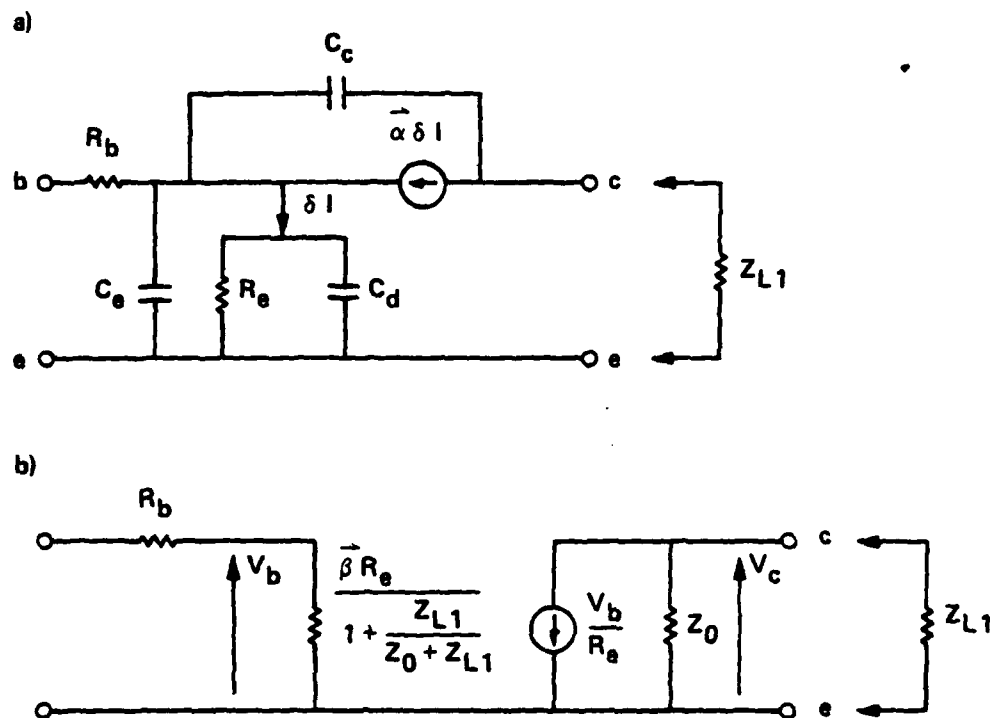
$$\vec{\beta} \equiv \frac{\beta_0}{1 + j\omega\beta_0/\omega_t} \qquad\qquad Z_0 \equiv \frac{1}{j\omega\vec{\beta}C_c}$$

$\omega_t/2\pi =$ cut off frequency of transistor in Hz

$\beta_0 =$ DC common emitter current gain

$C_c =$ collector-base capacitance

Fig. 19 High-frequency model of bipolar transistor:
      a) Basic model (Ref. 21)
      b) Equivalent model.

occurs when both transistors are driven hard (so that $R_{e2} \ll R_L$ and $|\beta R_e| \ll 2R_f$). The maximum high frequency rolloff of the transimpedance amplifier is then at

$$f_{3db} = \frac{1}{2\pi(2R_f C_c)} \qquad (4.11)$$

This is an upper limit, since it may not be possible or desirable to drive the transistors too hard; (e.g., so as not to exceed maximum current ratings or cause excessive noise). Furthermore, there is an additional bandwidth constraint determined by the input RC time constant. Using Eq. (4.3), this is

$$f'_{3dB} \approx \frac{1}{2\pi C_s R_f/|G|} \qquad (4.12)$$

where C_s is the capacitance of the source (APD + stray) and where we have assumed that G is approximately real (which it is for $\omega \gg \omega_t/\beta_0$). Usually, Eq. (4.11) dominates the determination of the bandwidth rather than Eq. (4.12); i.e., the bandwidth is usually determined by the amplifier speed rather than the input RC time constant. Good agreement with experiment has been found.

The actual circuit that was used in the modules for the contract hardware requirements is shown in Fig. 20. This is essentially the same as Fig. 18 with bias circuitry added. However, there are a few differences. The 270Ω resistor at the base of the output transistor has been added to improve stability[22] by decreasing the gain at very high frequencies. The 47Ω resistor at the output has been added to increase the bandwidth (by ~25%) by increasing R_L in Eq. (4.10); this resistor nearly halves the closed loop gain at the output terminal (in volts/amp) for a 50-ohm load, but has the desirable effect of stabilizing the amplifier against capacitance loading (e.g., a filter). The resistor causes the output

a)

$V_{detector}$ ≈ + 7V

.005
(200V)   .005 (200V)

50K   .01
(200V) .18

430

50K

5K

.039
(200V)

270

NE 68335

270

NE 68335

1.0   47

V_{out}

detector

R_f

Thick film chip resistors by Varadyne.
Chip capacitors by Johanson Dielectrics.
Bipolar transistors by NEC

b)

R_f R_f ~ 1 K Ω
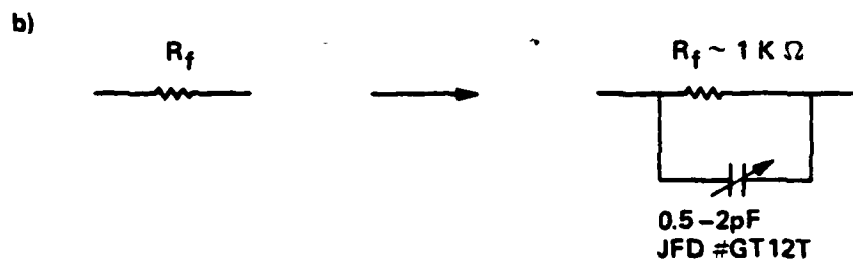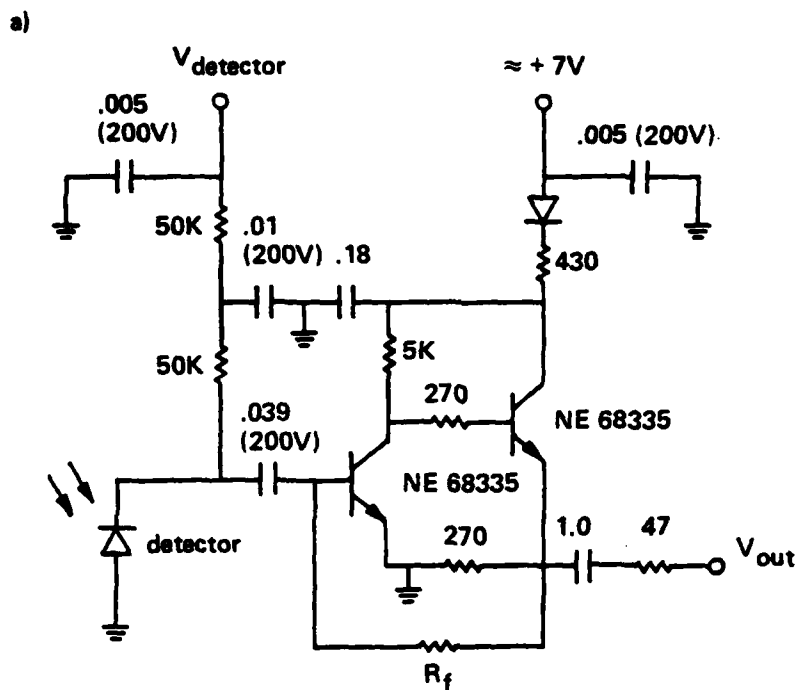
0.5 – 2pF
JFD #GT12T

Fig. 20   Varian APD preamp module circuit.
        a)   Circuit schematic.
        b)   Modification for larger bandwidths.

impedance to be about 50 ohms, which is also desirable. As shown in Fig. 20b, R_f may be shunted with a small capacitor if very large band-widths are needed (which require smaller R_f). This is to flatten out a peak in frequency response that would otherwise occur at high frequencies.

The amplifier of Fig. 20 has the gain saturate when the output voltage is somewhat larger than 100 mV (independent of R_f). This occurs at a photocurrent of

$$I_{sat} \simeq 0.1V/(R_f/2) \xrightarrow[\;R_f = 7\ K\Omega\;]{} 30\ \mu A \qquad (4.13)$$

$$\xrightarrow[\;R_f = 1\ K\Omega\;]{} 200\ \mu A \qquad .$$

Such values of I_{sat} result in a dynamic range of about 32 dB.

4.1.3   Noise Analysis of Transimpedance Amplifier

Generally, amplifiers have noise which can be represented by a combination of voltage noise generators and current noise generators at the input of a noiseless amplifier. This representation often obscures the relative importance of various noise sources. However, it has been found that it is relatively easy to compare the importance of various noise sources if one assigns an effective noise resistance R^* to a noise source such that a current noise generator, I_n, placed in parallel with the detector at the input, correctly describes that noise when I_n is taken to be the Johnson thermal noise current of the resistance R^*; i.e.,

$$I_n^2 = 4kT\ B/R^* \qquad (4.14)$$

(B = effective noise bandwidth in Hz).

For multiple noise sources, the corresponding effective noise resistances combine in parallel. The total noise current is then the Johnson noise of the equivalent parallel resistance. Hence, knowing the R^* of each noise source allows the total noise current to be calculated from the Johnson noise of $R^* = R_1^* || R_2^* || R_3^* || R_4^*$ ...... Hence the most important noise sources are easily identified as those having the smallest effective noise resistances. The r.m.s. noise current I_n of Eq. (4.14) adds directly to the photocurrent signal I_s generated in the detector. Hence the signal-to-noise ratio is simply $(I_s/I_n)^2$.

Effective noise resistances for the transimpedance amplifier arise from the feedback resistance R_f and from the shot noise of the base and collector currents. The effective noise resistance for R_f is simply

$$R_f^* = R_f \quad , \tag{4.15}$$

while for a bipolar transistor[23]

$$R_{BIP}^* = R_b^* || R_c^* \quad \underset{\text{at optimum bias}}{\frac{\sqrt{3}\beta_0}{2\pi \, nC_{in} \, B}} \quad , \tag{4.16}$$

where the base current shot noise has the associated noise resistance

$$R_b^* = 2kT \, \beta_0/qI_e = \frac{2}{n} \beta_0 R_e \quad , \tag{4.17}$$

while the collector current shot noise has the associated noise resistance

$$R_c^* \approx \frac{6}{\bar{n} \, R_e \, (2\pi \, C_{in} \, B)^2} \quad . \tag{4.18}$$

Here, B is the bandwidth for an assumed sharp cutoff at B Hz. C_{in} is
the total capacitance at the input of the preamp and includes both the
photodiode capacitance C_{PD} and the input capacitance of the input trans-
istor. β_0 is the DC current gain and n is the nonideality factor of the
emitter-base junction (for microwave transistors n $\approx$ 1.5); R_e is the
differential DC resistance of the emitter-base p-n junction and is
related to the emitter current I_e by $R_e = nkT/I_e$. The noise of a bipolar
transistor (eqs. (4.10)-(4.18)) is minimized when R_e is adjusted (via
I_e) so that $R_b^* = R_c^*$. This results in the optimum value of R_{BIP}^* shown on
the far right side of Eq. (4.16).

Some magnitude estimates may be helpful.

$$R_{BIP}^* \xrightarrow[\substack{\beta_0 = 100,\ n = 1.5 \\ C_{in} = 5\ pF \\ B = 50\ MHz}]{} 7.4\ K\Omega \qquad (4.19)$$

which occurs at I_e = 0.34 mA. Most transistors do not operate well at
such low currents.

If R_f = 7 KΩ is chosen, then the total noise resistance of the
amplifier is

$$R^* = R_f || R_{BIP}^* = 3.6\ K\Omega \qquad (4.20)$$

which by Eq. (4.14) has

$$I_n/\sqrt{B} = 2.1\ pA/\sqrt{Hz} \qquad \cdot \qquad (4.21)$$

For a microwave transistor with C_c = 0.2 pF, a bandwidth of 57 MHz would
be expected by Eq. (4.11).

43

Finally, it is of interest to know whether the APD dark current I_D makes a negligible contribution to noise. If the dark current has been multiplied in the same way as the photocurrent, the effective noise resistance is

$$R_D^* = 2kT/qI_DFM \xrightarrow[\substack{I_D = 10 \text{ nA} \\ F/M = 0.42 \\ M = 25}]{} 19 \text{ K}\Omega \quad . \quad (4.22)$$

On the right side of this expression, we have used values for a Type I APD. Note that $R_D^* \gg R^*$ of Eq. (4.20) for the preamp, and so the dark current makes a negligible contribution to the noise.

4.1.4   Three-Transistor Bipolar Transimpedance Amplifier

We have also fabricated the three-transistor amplifier of Fig. 21. This amplifier has a grounded emitter transistor at the input driving a grounded base transistor which is then followed by an emitter-follower transistor. Such amplifiers achieve more voltage gain because a grounded base transistor can drive a larger load than a grounded emitter amplifier, since the grounded base transistor has an output impedance of $1/j\omega C_c$, while the grounded emitter transistor has an output impedance of $1/j\omega\vec{\beta}C_c$. The larger gain would allow a larger value of R_f to be used before the bandwidth becomes constrained by Eq. (4.12); (Eq. (4.11) is not valid for this amplifier.) Larger R_f decreases the noise. On the other hand, voltage gain is delayed until the second stage (i.e., the grounded base transistor), so that the second stage noise now becomes important. The result is to decrease R_c^* of Eq. (4.18) by a factor of 2 which decreases R_{BIP}^* at optimum bias by a factor of $\sqrt{2}$.

In practice, we have found that the three-transistor amplifier for a given bandwidth is slightly noisier than the two-transistor amplifier.
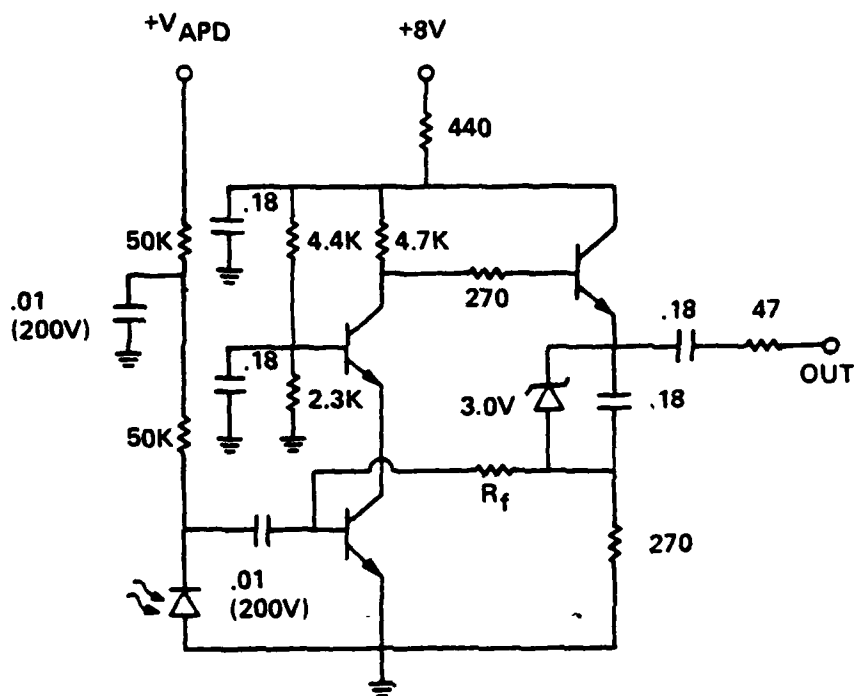
Fig. 21   Three-transistor bipolar transimpedance amplifier.

Furthermore, since we have obtained very large bandwidths (up to 450 MHz with R_f = 1 KΩ) with the two-transistor preamp, there is no need to use the three-transistor preamp. Hence we have chosen the two-transistor preamp for our APD modules, even though the three-transistor preamps typically have about 25% larger bandwidth than the two-transistor preamps for the same value of R_f.

4.2 Preamp Results and Module Performance

Some finished preamp modules are shown in Figs. 22 and 23. The APDs are packaged in the micro-window packages which Fig. 8 are then inserted into a SMA-type bulkhead mount, using simple hardware. The APDs are removeable and can be interchanged. Figures 22 and 23 also show an alternative version of the modules that has the APD permanently mounted on the PC board.

As our circuit analysis shows, in order to obtain optimum preamp performance, microwave transistors that operate well at submilliamp collector currents and that have small collector-base capacitance are required. Microwave transistors are required in order to have small capacitance and in order to have decent voltage gain at high frequencies (so that Eq. (4.12) does not restrict the bandwidth). They must have very small collector-base capacitance to have large bandwidth (Eq. (4.11)). They must operate well at submilliamp currents in order to minimize noise. Hence very small-area microwave transistors are required. An ideal choice for such transistors is the NEC transistor NE68335, which has peak performance at about 0.8 mA, and which has $C_c \approx 0.2$ pF and f_t = 5 GHz. For this transistor, the preamp modules have a capacitance to ground at the base input of $C_{in} \approx 5$ pF, which consists of 1.0 pF from the APD chip, 0.3 pF from the APD micro-window package, 1.8 pF from the APD package mounting connector and hardware, 1.5 pF from the input transistor (including the Miller effect) and 0.4 pF stray capacitance on the PC board.
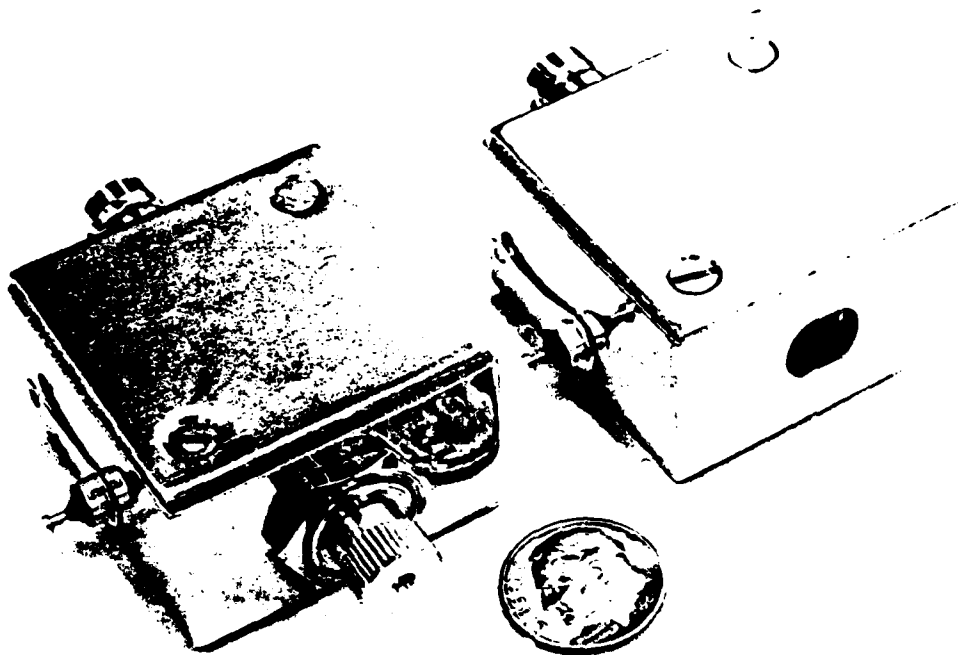
46

Fig. 22   Varian APD/preamp modules (exterior view). The model on the
          right has the APD as a permanent part of the circuit, while
          the module on the left allows the APD to be removed and
          replaced with other similarly packaged APDs.
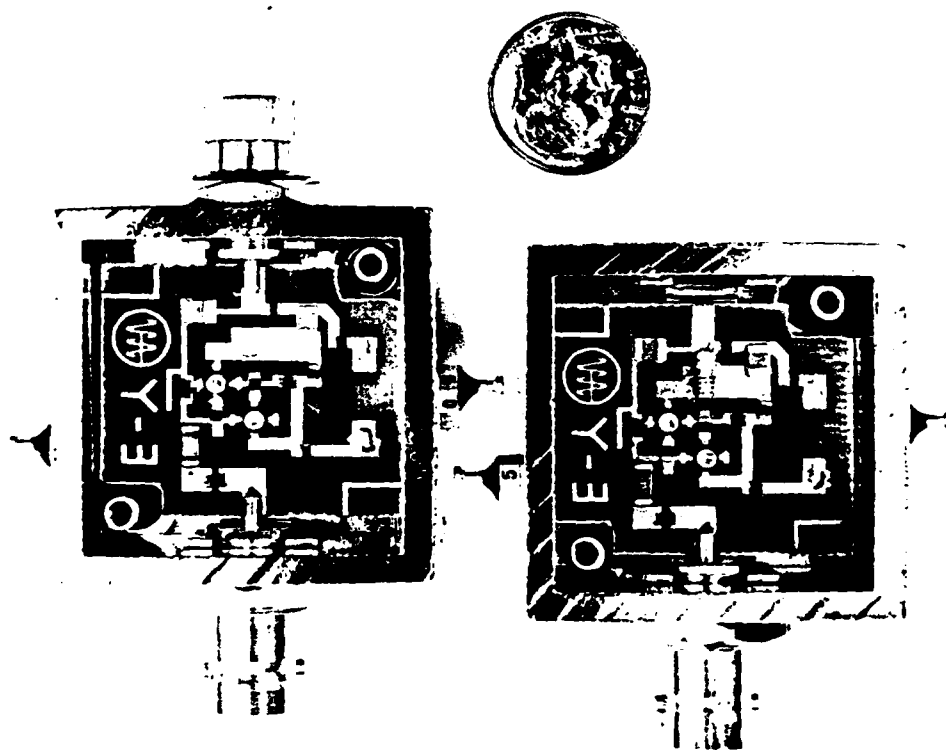
47

Fig. 23   Varian APD/preamp module (interior view). The model on the
          right has the APD as a permanent part of the circuit, while
          the module on the left allows the APD to be removed and
          replaced with other similarly packaged APDs.

48

Ten modules were delivered under this contract. The characteristics of these preamps are shown in Fig. 24. Modules #1-8 have R_f = 7 KΩ and about a 52-MHz bandwidth. Modules #9-10 have R_f = 1 KΩ shunted by ~0.5 pF. The shunt capacitance was chosen to reduce the bandwidth for modules #9-10 to about 250 MHz. (Smaller shunt capacitance would allow flat response within a bandwidth of 450 MHz.)

As discussed below Eq. (4.21), preamps #1-8 are expected to have a bandwidth of about 57 MHz and an equivalent input noise current of $I_n/\sqrt{B}$ = 2.1 pA/$\sqrt{Hz}$. Similarly, preamps #9-10 are expected to have a maximum bandwidth of 400 MHz, with $I_n/\sqrt{B}$ = 5.2 pA/$\sqrt{Hz}$ for a reduced bandwidth of 250 MHz.

As Fig. 24 shows, the predicted bandwidths are accurate. (Preamps 9-10 have a bandwidth of 450 MHz if R_f is shunted with ~0.3 pF.) On the other hand, all preamps have values of $I_n/\sqrt{B}$ that are noisier than expected by a factor of about 1.7 (Fig. 24). Much of this discrepancy is probably due to the very non-white nature of the noise, which results in the noise bandwidth being substantially larger than the signal band-width, even when a 12-dB/octave filter has been used to limit the bandwidth. (The theoretical predictions are based on a sharp high-frequency cutoff.) This problem is accentuated by the fact that the most important noise source at higher frequencies is not white, but increases as ω^2. Part of the noise prediction discrepancy may also be due to the inadequacy of the simple transistor model that has been employed.

The bandwidth measurements were performed by removing the APD from the module and using the SMA APD mounting connector on the module to connect a 4-pF, 1-KΩ current source that could be sinusoidally modulated with a variable frequency signal of known (constant) amplitude. Moni-toring the sinusoidal signal at the output on either an oscilloscope or a power meter as the frequency was varied, then allowed f_{3dB} to be determined. The rise and fall times of the amplifiers could also be

Fig. 24   VARIAN PREAMP MODULE CHARACTERISTICS

Preamp No.	Preamp Operating Voltage	1) Preamp Bandwidth (MHz)	1) Preamp Risetime/ Falltime (nsec)	1,2) Preamp gain (V_{out}/I_{in}) (mV/µA)	1,3,4) Equivalent Input noise current, $I_n/\sqrt{B}$ (pA/√Hz)	1,3-5) NEP (pW/√Hz) 6)
1	7	0.002 - 52	6.5	3.0	3.6	0.35 6)
2	7	0.002 - 50	6.5	2.9	3.5	3.4
3	7	0.002 - 54	6.5	3.1	3.5	2.9
4	7	0.002 - 53	6.5	2.9	3.6	3.3
5	7	0.002 - 51	6.5	2.9	3.6	3.4
6	7	0.002 - 52	6.5	2.9	3.6	3.4
7	7	0.002 - 51	6.5	3.0	3.6	3.2
8	7	0.002 - 55	6.5	3.0	3.6	3.7
9	8	0.002 - 250	1.4	0.550	8.6	7.8
10	8	0.002 - 260	1.3	0.525	8.8	7.6

Notes:

1) Assumes module is operated into 50Ω.

2) Gain may saturate if $|V_{out}| > 100$ mV.

3) Preamp is loaded with similarly numbered APD (see Fig. 2); e.g., APD No. 1 is in preamp No. 1, etc.

4) Based on broadband noise after the full bandwidth was reduced by 20% using a 12-dB/octave filter. I_n is 15% higher if the bandwidth is reduced by only 4% by the 12-dB/octave filter. The APD is present and biased near breakdown. If the APD is omitted, I_n decreases by about 20% due to reduction of input capacitance.

5) For λ = 1.1 µm. APDs are biased to optimum gain, as indicated in Fig. 2 .

6) Operating at 23°C and 75.60V, where M = 24. This is the optimum operating point for this APD for low bit error rates. For higher bit error rates, this APD may be operated at M up to 35. At M = 35, the NEP is 0.26 pW/√Hz.

determined by illuminating the APD/preamp module containing a Type II
APD with a fast rectangular pulse from an InGaAsP laser. The pulse
response of preamp #9 is shown in Fig. 25. The rise and fall times are
1.4 nsec, which is consistent with the f_{3dB} measurements (rise time
$\approx 1/3f_{3dB}$).

The amplifier noise measurements were obtained using the shot noise
of a known photocurrent, I_{PH}, to calibrate the measurement system. With
the APD biased at about half the breakdown voltage (so that $F = M = 1$),
one measures the (amplified) output power in the dark (P_D) and also
under illumination ($P_{D + PH}$). Without the need to know the amplifier
gain or the noise bandwidth, one then obtains

$$\frac{I_n^2}{B} = \frac{2q\,I_{PH}}{(P_{D+PH}/P_D) - 1} \tag{4.23}$$

The NEP of the Type II APDs (+ preamps) is readily obtained, since
at the (low) optimum gain (shown in Fig. 14) the photocurrent does not
contribute to the noise. The NEP is then simply given by Eq. (3.4b) in
terms of $I_n/\sqrt{B}$. The NEP values are shown in Fig. 24 and range from
2.9 pW/$\sqrt{Hz}$ for a 54-MHz bandwidth module to 7.6 pW/$\sqrt{Hz}$ for a 260-MHz
module.

For the Type I APD operating at $M = 24$ (which is optimum gain for a
high signal-to-noise ratio and low b.e.r.), the NEP is given by Eq.
(3.4) and has a value of 0.35 pW/$\sqrt{Hz}$. For higher error rates, the Type
I APD could be operated up to $M = 35$, where Eq. (3.4a) gives an NEP
value of 0.26 pW/$\sqrt{Hz}$. (The NEP values have been given for a wavelength
of 1.1 μm.) Operated at $M = 24$, the Type I APD improves the NEP by 14
dB over the NEP of the same diode operated at $M = 1$. This demonstrates
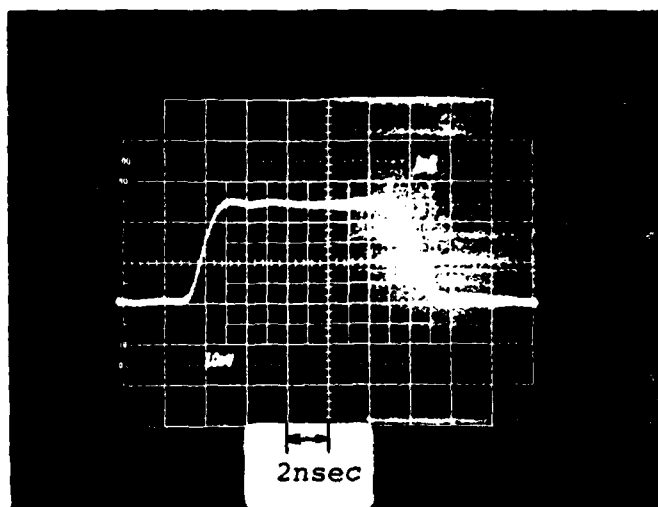that the APD gain is indeed useful for improving sensitivity.

Fig. 25   Pulse response of transimpedance amplifier.
The rise time is 1.4 nsec.

52

5.   SUMMARY AND CONCLUSIONS

With the successful fabrication of high-performance (Type I) hybrid InP-InGaAsP APDs, it is apparent that the avalanche gain improves sensitivity by about 11-14 dB (depending on b.e.r. required) over nonavalanching photodiodes. Such APDs used with simple bipolar preamps have sensitivity slightly better than the recently-described[19,20] nonavalanching pin-FET receiver modules. The disadvantage of an APD is the need for an accurate, high-voltage, temperature-compensated APD bias supply; however, there are many advantages. The advantages of the APD/bipolar preamp over pin-FET modules are its much greater dynamic range, its extended low-frequency response (near DC), its low 1/f noise, its non-requiring equalization, and its ability to work well at elevated temperatures. (The gate leakage current of MESFETs is likely to be a problem at higher temperatures (~50°C) for the pin-FET modules.)

If hybrid APDs were easier to make, there undoubtedly would be less interest in the pin-FET receivers. It seems quite premature to assume that fabrication and yield problems cannot be solved, since work on hybrid APDs has only recently begun. On the other hand, hybrid APDs are presently quite difficult to make, while nonavalanching photodiodes are comparatively straightforward. The future is likely to see both APDs and nonavalanching photodiodes being used for long-wavelength optical fiber communications, with nonavalanching photodiodes being dominant in the near future.

6.   REFERENCES

1. C. E. Hurwitz and J. J. Hsieh, Appl. Phys. Lett. 32, 487 (1978).

2. H. D. Law, L. R. Tomasetta and K. Nakano, Appl. Phys. Lett. 33, 920 (1978).

3. R. Yeats and S. H. Chiao, Appl. Phys. Lett. 34, 581 (1979).

4. R. Yeats and S. H. Chiao, Appl. Phys. Lett. 36, 167 (1980).

5. Y. Matsushima, K. Sakai, S. Akiba and T. Yamamoto, Appl. Phys. Lett. 35, 466 (1979).

6. K. Taguchi, Y. Matsumoto and K. Nishida, Electron. Lett. 15, 453 (1979).

7. K. Nishida, K. Taguchi and Y. Matsumoto, Appl. Phys. Lett. 35, 251 (1979).

8. C. A. Armiento, S. H. Groves and C. E. Hurwitz, Appl. Phys. Lett. 35, 333 (1979).

9. T. P. Lee, C. A. Burrus, A. G. Dentai, A. A. Ballman and W. A. Bonner, Appl. Phys. Lett. 35, 511 (1979).

10. S. R. Forrest, M. DiDomenico, Jr., R. G. Smith and H. J. Stocker, Appl. Phys. Lett. 36, 580 (1980).

11. R. J. McIntyre, IEEE Trans. Electron. Devices ED-19, 703 (1972).

12. R. Yeats and S. H. Chiao, "III-V Heterostructure Avalanche Photo-diode Modules for Fiber Optic Communication Links in the 1.0 to 1.3 Micrometer Spectral Range," Interim Report No. 1, U.S. Army Communications R&D Command, Fort Monmouth, NJ, Contract DAAB07-78-C-2402, (September 1978).

13. R. Yeats and S. H. Chiao, Interim Report No. 2 (as in Ref. 12) (April 1979).

14. R. Yeats, Interim Report No. 3 (as in Ref. 12) (September 1979).

15. V. Diadiuk, S. H. Groves, C. E. Hurwitz, Appl. Phys. Lett. 37, 807 (1980).

16. Monthly Progress Report #13 of this contract.

17. Specifically, Eq. (3) in H. Melchior, W. T. Lynch, IEEE Trans. Electron. Devices ED-13, 829 (1966).

18. R. Yeats and K. Von Dessonneck, "Long Wavelength Detectors for Optical Fiber Communications," High-Speed Photodetectors, Proc. Soc. Photo-Opt. Instr. Eng. 272, (1981).

19. R. C. Hooper, D. R. Smith, B. R. White, "Pin-FET Hybrids for Digital Optical Receivers," presented at IEEE Electron. Components Conf., San Francisco (April 1980).

20. D. R. Smith, R. C. Hooper, K. Ahmad, D. Jenkins, A. W. Mabbitt and R. Nicklin, Electron. Lett. 16, 69 (1980).

21. J. E. Carroll, Physical Models for Semiconductor Devices (Crane, Russak & Co., Inc. NY) 103 (1974).

22. R. G. Smith, C. A. Brackett, H. W. Reinbold, Bell Sys. Tech. J. 57, 1809 (1978).

23. Expressions for noise resistance may be inferred, for example, from S. D. Personick, Proc. IEEE 65, 1670 (1977).

APPENDIX A: SENSITIVITY ANALYSIS

Symbols:

P_R = optical power hitting APD

$h\nu$ = photon energy

q = electronic charge

η = quantum efficiency

B = <u>noise</u> bandwidth of receiver in Hz. For a single pole roll-off, $B = \frac{\pi}{2} \times f_{3dB}$. B is about half the allowed bit rate.

b.e.r. = bit error rate

SNR = signal-to-noise ratio of electrical <u>power</u> referred to the input of the preamp. SNR $\approx$ 36 for 10^{-9} b.e.r.

NEP = noise equivalent power = $P_R B^{-1/2}$ for a signal power P_R causing a SNR $= 1$

M = photocurrent gain

I_1 = primary dark current that gets multiplied

I_0 = average primary photocurrent that generates desired SNR when dark current is negligible ($I_1 \ll I_0$)

I_0' = average primary photocurrent that generates desired SNR when dark current dominates photocurrent ($I_1 \gg I_0$)

P_R' = optical power corresponding to I_0'

$F(M)$ = excess noise factor, a function of M

$\alpha(\beta)$ = electron (hole) ionization coefficients

K = F/M; $K \approx \beta/\alpha$ (or α/β) for electron (or hole) initiation of the avalanche, respectively.

I_n =   equivalent rms input noise current of preamp (in amps)

$I_{n,APD}$ =   equivalent rms noise current of APD (in amps)

Analysis of the sensitivity requires knowledge of F, the excess noise factor of the APD. F is given by[*]

$$F = M \left[1 - (1 - K) \left(\frac{M}{M - 1} \right)^2 \right] \tag{A-1}$$

$$\approx KM \quad \text{(for } M \gg 1/K) \quad , \tag{A-2}$$

where K is a suitably averaged[*] ratio of ionization coefficients; $K = \beta/\alpha$ if electrons initiate the avalanche, or $K = \alpha/\beta$ if holes initiate the avalanche.

Assuming the dark current is multiplied the same was as the photo-current gives the APD noise:[*]

$$I_{n,APD}^2 = 2qB \, M^2 F \, (I_0 + I_1) \quad , \tag{A-3}$$

where the primary photocurrent is

$$I_0 = \eta q P_R / h\nu \quad . \tag{A-4}$$

The signal-to-noise ratio (of power) is then

$$SNR = \frac{(M \, I_0)^2}{I_{n,APD}^2 + I_n^2} \quad . \tag{A-5}$$

---

[*]R. J. McIntyre, IEEE Trans. Electron. Dev. ED-19, 703 (1972).

Using Eqs. (A-2) to (A-5), we find that SNR is maximized with respect to M when

$$I_{n, APD}^2 = 2I_n^2 \qquad\qquad (A-6)$$

Then

$$M_{opt} = \left[\frac{I_n^2}{qBK(I_0 + I_1)} \right]^{1/3} \qquad\qquad (A-7)$$

Equations (A-2) to (A-7) determine the sensitivity when the APD is biased to the optimum gain. There are 2 cases:

<u>Case (a)</u>. $I_1 \ll I_0$ (low dark current):

$$M_{opt} = (3\ SNR)^{-1/4} (I_n/qBK)^{1/2} \qquad\qquad (A-8)$$

and

$$I_0 \approx (3\ SNR)^{3/4} (qBKI_n)^{1/2} \quad , \qquad\qquad (A-9)$$

which corresponds to

$$P_R = \frac{h\nu}{\eta q} I_0 \qquad . \qquad\qquad (A-10)$$

The NEP, for optimum or non-optimum M, is

$$NEP = \frac{h\nu}{\eta q} \left\{ qMK\sqrt{B} + \sqrt{q^2 M^2 K^2 B + I_n^2/(M^2 B)} \right\} \qquad\qquad (A-11)$$

$$\xrightarrow{M \ll M_{opt}} \frac{h\nu}{\eta q} \frac{I_n}{M\sqrt{B}} \qquad . \qquad\qquad (A-12)$$

58

Case (b): $I_1 \gg I_0$ (large dark current):

$$M_{opt} = \left[\frac{I_n^2}{q\beta K I_1}\right]^{1/3} \tag{A-13}$$

and

$$I_0' = \left(\frac{I_1}{I_0}\right)^{1/3} I_0 \quad , \tag{A-14}$$

which corresponds to

$$P_R' = \left(\frac{h\nu}{\eta q}\right) I_0' = \left(\frac{I_1}{I_0}\right)^{1/3} P_R \quad . \tag{A-15}$$

In Eq. (A-14), I_0 is given by Eq. (A-9) and P_R is given in Eq. (A-10). Equation (A-15) shows that large dark current degrades the sensitivity by $(I_1/I_0)^{1/3}$.

DISTRIBUTION LIST

Defense Documentation Center
ATTN: DTIC-TCA
Cameron Station (Bldg. 5)
Alexandria, VA 22314

Director
National Security Agency
ATTN: TDL
Fort George G. Meade, MD 20755

DCA Defense Comm. Engrg. Ctr.
Code R123, Tech Library
1860 Wiehle Ave.
Reston, VA 22090

Defense Communication Agency
Technical Library Center
Code 205 (P. A. Tolovi)
Washington, DC 20305

Office of Naval Research
Code 427
Arlington, VA 22217

GIDEP Engineering & Support Dept.
TE Section
P. O. Box 398
Norco, CA 91760

Director
Naval Research Laboratory
ATTN: Code 2627
Washington, DC 20375

Commander
Naval Electronics Laboratory Center
ATTN: Library
San Diego, CA 92152

Cdr., Naval Surface Weapons Center
White Oak Laboratory
ATTN: Library, Code WX-21
Silver Springs, MD 20910

Commandant, Marine Corps
HQ, US Marine Corps
ATTN: Code LMC
Washington, DC 20380

HQ, US Marine Corps
ATTN: Code LNTS
Washington, DC 20380

Command, Control & Communications Div.
Development Center
Marine Corps Development & Educ. Cdmd.
Quantico, VA 22134

Naval Telecommunications Command
Technical Library Code 91L
4401 Massachusetts Avenue, NW
Washington, DC 20390

Naval Air Systems Command
Code: AIR-5332
Washington, DC 20360

AUL/LSE 64-285
Maxwell AFB, AL 36112

Rome Air Development Center
ATTN: Documents Library (TILD)
Griffiss AFB, NY 13441

Air Force Geophysics Lab
L. G. Hanscom AFB
ATTN: Lib
Bedford, MA 01730

HQ, ESD (DRI)
L. G. Hanscom AFB
Bedford, MA 01731

HQ, Air Force Electronic Warfare Ctr.
ATTN: SURP
San Antonio, TX 78243

HQ, Air Force Systems Command
ATTN: DLCA
Andrews AFB
Washington, DC 20331

Director
US Army Materials Systems Analysis Acty.
ATTN: DRXSY-T
Aberdeen Proving Ground, MD 21005

Cdr., MIRADCOM
Redstone Scientific Info Center
ATTN: Chief, Document Section
Redstone Arsenal, AL 35809

Commander
US Army Intelligence Center
  & School
ATTN: ATSI-CD-MD
Fort Huachuca, AZ 85613

Commander
HQ Fort Huachuca
ATTN: Technical Reference Div.
Fort Huachuca, AZ 85613

Commander
USASA Test & Evaluation Center
ATTN: IAS-CDR-T
Fort Huachuca, AZ 85613

Dir., US Army Air Mobility R&D Lab
ATTN: T. Gossett, Bldg. 207-5
NASA Ames Research Center
Moffett Field, CA 94035

HQDA (DAMO-TCE)
Washington, DC 20310

Deputy for Science & Technology
Office, Asst. Sec. Army (R&D)
Washington, DC 20310

HQDA (DAMA-ARP)
Dr. F. D. Verderame
Washington, DC 20310

Cdr., Harry Diamond Labs
ATTN: Library
2800 Powder Mill Road
Adelphi, MD 20783

Director
US Army Ballistic Research Labs
ATTN: DRXBR-LB
Aberdeen Proving Ground, MD 21005

Director
US Army Ballistic Research Labs
ATTN: DRXBR-CA
(Dr. L. Vandekieft)
Aberdeen Proving Ground, MD 21005

Cdr., AVRADCOM
ATTN: DRSAV-E
P. O. Box 209
St. Louis, MO 63166

Commander
Picatinny Arsenal
ATTN: SARPA-ND-A-4 (Bldg. 95)
Dover, NJ 07801

Director
Joint Comm. Office (TRI-TAC)
ATTN: TT-AD (Tech. Docu. Ctr.)
Fort Monmouth, NJ 07703

Project Manager, REMBASS
ATTN: DRCPM-RBS
Fort Monmouth, NJ 07703

Project Manager, NAVCON
ATTN: DRCPM-NC-TM
Bldg. 2539
Fort Monmouth, NJ 07703

Commander
US Army Satellite Communications Agency
ATTN: DRCPM-SC-3
Fort Monmouth, NJ 07703

Cdr., US Army Research Office
ATTN: DRXRO-IP
P. O. Box 12211
Research Triangle Park, NC 27709

Cdr., US Army Tropic Test Center
ATTN: STETC-MO-A (Tech Library)
Drawer 942
Fort Clayton, Canal Zone 09827

Commander, DARCOM
ATTN: DRCDE
5001 Eisenhower Avenue
Alexandria, VA 22333

Cdr., US Army Signals Warfare Lab
ATTN: DELSW-OS
Arlington Hall Station
Arlington, VA 22212

Bell Telephone Laboratory
ATTN: Dr. R. Nahory
Holmdel, NJ 07733

Commander
US Army Training & Doctrine Command
ATTN: ATCD-TEC
Fort Monroe, VA 23651

Director, Night Vision Laboratory
US Army Electronics R&D Command
ATTN: DELNV
Fort Belvoir, VA 22060

Commander
US Army ERADCOM
NV/EO Lab
Attn: Dr. R. G. Buser
Fort Belvoir, VA 22060

Cdr/Dir Atmospheric Sciences Lab
US Army Electronics Command
ATTN: DRSEL-BL-SY-S
White Sands Missile Range, NM 88002

Chief, Aviation Electronics Div (SIMO)
US Army Electronics Command
ATTN: DRSEL-SI-AE
P. O. Box 209
St. Louis, MO 63166

Chief,
Intel Material Dev. & Support Office
Electronic Warfare Lab, ECOM
Fort Meade, MD 20755

Hanscom AFB
Attn: Dr. Eirug Daview (ESO)
Deputy for Electronic Technology
Bedford, MA 01730

MIT - Lincoln Laboratory
ATTN: Library (RM A-082)
P. O. Box 73
Lexington, MA 02173

NASA Scientific & Technical
  Information Facility
P. O. Box 8757
Baltimore/Washington Intl. Airport
Baltimore, MD 21240

Advisory Group on Electron Devices
201 Varick Street, 9th Floor
New York, NY 10014

Advisory Group on Electron
  Devices
ATTN: Secy, Working Group D
201 Varick Street
New York, NY 10014

TACTEC
Battelle Memorial Institute
505 King Avenue
Columbus, OH 43201

Ketron, Inc.
ATTN: Mr. Frederick Leuppert
1400 Wilson Blvd., Architect Bldg.
Arlington, VA 22209

R. C. Hansen, Inc.
P. O. Box 215
Tarzana, CA 91356

Wright Patterson AFB
ATTN: Dr. D. J. Peacock
AFAL/DHO, Ohio 46433

Naval Ocean Systems Center
ATTN: Dr. W. Putnam
Code 8115
San Diego, CA 92152

Naval Ocean Systems Center
ATTN: Dr. Steve Miller, Code 922
San Diego, CA 92152

Laser Diode Labs
ATTN: Dr. T. Stockton
1130 Somerset Street
New Brunswick, NJ 08901

Rockwell International Science Ctr.
ATTN: Dr. L. Tomasetta
1049 Camino Dos Rios
P. O. Box 1085
Thousand Oaks, CA 91360

Spectronics
Attn: Dr. H. A. Allen
830 East Anapaho Road
Richardson, TX 75081